Exploring the role of composition and mass loading on the properties of hadronic jets

Monthly Notices of the ROYAL ASTRONOMICAL SOCIETY

MNRAS **520,** 6017–6039 (2023) https://doi.org/10.1093/mnras/stad521
Advance Access publication 2023 February 16

Exploring the role of composition and mass loading on the properties of hadronic jets

D. Kantzas [1,2★†], S. Markoff [1,2], M. Lucchini [3], C. Ceccobello[4] and K. Chatterjee [5]

[1]*Anton Pannekoek Institute for Astronomy (API), University of Amsterdam, Science Park 904, NL-1098 XH Amsterdam, the Netherlands*
[2]*GRavitation AstroParticle Physics Amsterdam (GRAPPA), University of Amsterdam, Science Park 904, NL-1098 XH Amsterdam, the Netherlands*
[3]*MIT Kavli Institute for Astrophysics and Space Research, Massachusetts Institute of Technology, Cambridge, MA 02139, USA*
[4]*Department of Space, Earth and Environment, Chalmers University of Technology, Onsala Space Observatory, SE-439 92 Onsala, Sweden*
[5]*Black Hole Initiative at Harvard University, 20 Garden Street, Cambridge, MA 02138, USA*

Accepted 2023 February 13. Received 2023 February 13; in original form 2022 July 6

ABSTRACT

Astrophysical jets are relativistic outflows that remain collimated for remarkably many orders of magnitude. Despite decades of research, the origin of cosmic rays (CRs) remains unclear, but jets launched by both supermassive black holes in the centre of galaxies and stellar-mass black holes harboured in X-ray binaries (BHXBs) are among the candidate sources for CR acceleration. When CRs accelerate in astrophysical jets, they initiate particle cascades that form γ-rays and neutrinos. In the so-called hadronic scenario, the population of accelerated CRs requires a significant amount of energy to properly explain the spectral constraints, similarly to a purely leptonic scenario. The amount of energy required often exceeds the Eddington limit or even the total energy available within the jets. The exact energy source for the accelerated protons is unclear, but due to energy conservation along the jets, it is believed to come from the jet itself via transfer of energy from the magnetic fields or kinetic energy from the outflow. To address this hadronic energy issue and to self-consistently evolve the energy flux along the flows, we explore a novel treatment for including hadronic content, in which instabilities along the jet/wind border play a critical role. We discuss the impact of the different jet compositions on the jet dynamics for a pair dominated and an electron-proton jet and, consequently, the emitted spectrum, accounting for both leptonic and hadronic processes. Finally, we discuss the implications of this mass-loading scenario to address the proton energy issue.

Key words: acceleration of particles – stars: jets – galaxies: jets.

1 INTRODUCTION

Accreting black holes can efficiently launch relativistic outflows, known as astrophysical jets, by converting gravitational energy to kinetic energy. Large-scale jets launched by supermassive black holes (SMBH) share some common physical laws to the small-scale jets launched by stellar-mass black holes in X-ray binaries (BHXBs; Heinz & Sunyaev 2003; Merloni, Heinz & Di Matteo 2003; Falcke, Körding & Markoff 2004), and hence black hole jets appear to be scale invariant in some of their properties. For example, SMBHs with masses of the order of $\sim 10^6 - 10^9$ M$_\odot$ power jets that remain collimated up to Mpc scales (Waggett, Warner & Baldwin 1977), whereas BHXBs with mass of the order of a few solar masses display jets that remain collimated up to sub-pc scales (Mirabel & Rodriguez 1994). Galactic BHXBs are of particular importance because they transition between different jetted and non-jetted states over human-like time-scales, giving us the chance to understand plasma evolution in extreme conditions and better probe jet physics (see e.g. Markoff, Falcke & Fender 2001; Markoff et al. 2003; Reig, Kylafis & Giannios 2003; Giannios, Kylafis & Psaltis 2004; Markoff, Nowak & Wilms 2005; Maitra et al. 2009; Vila & Romero 2010; Zdziarski et al. 2014; Connors et al. 2019; Lucchini et al. 2021).

The exact physical mechanism responsible for jet launching is not clear yet. On the one hand, the Blandford–Znajek mechanism (Blandford & Znajek 1977) describes a way to extract the rotational energy of a spinning black hole and power relativistic jets that can be pair-plasma dominated (see e.g. Broderick & Tchekhovskoy 2015; Parfrey, Philippov & Cerutti 2019). On the other hand, magnetic fields anchored in the accretion disc can launch baryon/proton/ion-dominated jets via the Blandford–Payne mechanism (Blandford & Payne 1982). The difference in jet composition from the two launching mechanisms would have an important impact on the interpretation of the spectral energy distribution (SED) observed from such black hole systems as well as the consideration of relativistic jets as candidate sources of cosmic rays (CRs).

CRs are charged particles that exhibit a large range of energies going up to ultra-high energies of the order of 10^{20} eV (The Pierre Auger Observatory et al. 2017; Abbasi et al. 2020). The detected CR spectrum shows two very prominent features, known as the 'knee' and the 'ankle' where the spectrum steepens and hardens, respectively. The 'knee' is observed at 10^{15} eV (PeV) and is likely to be the maximum energy that CR protons accelerated in Galactic sources can reach, but the identification of these particular sources remains a mystery despite the decades of studies. The 'ankle', located

★ E-mail: kantzas@lapth.cnrs.fr
† Currently at: LAPTh, CNRS, USMB, F-74940 Annecy, France

at $\sim 10^{18}$ eV (EeV), is where extragalactic sources are thought to start dominating the spectrum. The exact CR composition is not clear and strongly depends on the particle energy. GeV CRs primarily comprise of protons (∼99 per cent; Shikaze et al. 2007), with electrons and positrons mainly contributing to the rest of the spectrum. It is likely that heavier elements/ions accelerated in Galactic sources start dominating the CR spectrum between the 'knee' and the 'ankle' (Aloisio, Berezinsky & Gazizov 2012), beyond which the composition is unclear (Abbasi et al. 2019; Yushkov, Collaboration et al. 2019; Corstanje et al. 2021).

Similar to large-scale jets of active galactic nuclei (AGN), which are among the dominant candidate sources of the extragalactic CRs (Protheroe & Kazanas 1983), recent studies suggest the small-scale jets of BHXBs as potential CR acceleration sites (Romero et al. 2003; Fender, Maccarone & van Kesteren 2005; Cooper et al. 2020). There are currently only a few tens of Galactic BHXBs detected in the Milky Way (Tetarenko et al. 2016), but population-synthesis simulations (see e.g. Olejak et al. 2020) suggest that a few thousand black holes likely reside in the Galactic disc, in agreement with the recent X-ray observations of the Galactic centre by Hailey et al. (2018) and Mori et al. (2021). Based on such observations, Cooper et al. (2020) proposed that a few thousand BHXBs are capable of contributing to the observed CR spectrum above the 'knee'.

Whether or not BHXBs jets can indeed accelerate CRs up to the 'knee', and AGN jets beyond the 'ankle', strongly depends on two further issues: (1) Can astrophysical jets, in general, accelerate particles to high energies, and (2) are astrophysical jets actually comprised of protons and/or heavier elements? On the former, observations of non-thermal emission from radio bands (see e.g. Lister et al. 2016) up to GeV/TeV γ-rays from both SMBHs (see e.g. Lister et al. 2009) and BHXBs (see e.g. Zanin et al. 2016), suggest that both classes of jets can efficiently accelerate particles. Numerous numerical studies, moreover, suggest that jets can indeed be viable sites of particle acceleration either via shocks (Hillas 1984) or via magnetic reconnection (Drenkhahn & Spruit 2002; Guo et al. 2014; Sironi & Spitkovsky 2014; Matthews, Bell & Blundell 2020).

The jet composition however remains an open question. The two different proposed launching mechanisms mentioned above yield an entirely different jet content at the base that significantly alters not only the jet dynamics, but the emitted spectrum as well (Petropoulou et al. 2019). A pair-dominated jet would allow only for leptonic processes, such as synchrotron and inverse Compton scattering (ICS; Blumenthal & Gould 1970). A leptonic plus hadronic jet, on the other hand, allows for further non-thermal processes, when inelastic collisions occur between the accelerated protons and the cold flow or radiation (e.g. Mannheim 1993; Rachen & Biermann 1993; Mannheim & Schlickeiser 1994; Rachen & Mészáros 1998). Such hadronic processes can lead to the production of astrophysical neutrinos, but usually require a much larger jet energy budget than the leptonic ones, sometimes requiring super-Eddington jet powers (Böttcher et al. 2013; Liodakis & Petropoulou 2020). Such super-Eddington powers challenge the accretion paradigm (Zdziarski & Böttcher 2015), but they still seem feasible for relativistic AGN jets (Ghisellini et al. 2014).

Several BHXB jets, such as the peculiar case of SS433 or the prototypical Cygnus X–1, show evidence of baryonic jet content (Fabrika 2004 and Gallo et al. 2005; Heinz 2006, respectively). Both the compact objects of SS433 and Cygnus X–1 are accompanied by a high mass donor star that may be the source of the heavy composition through its stellar wind. There is evidence of baryon-loaded jets though, even in the case of a low-mass companion, such as the black hole candidate 4U 1630–47, based on iron emission lines (Díaz Trigo et al. 2013). The cases of MAXI J1820+070 (Tetarenko et al. 2021; Zdziarski, Tetarenko & Sikora 2022a), MAXI J1836-194 (Lucchini et al. 2021), XTE J1752–223, MAXI J1659–152, and XTE J1650–500 (Cao et al. 2021) on the other hand, favour a jet composition of the order of a few to a few tens of pairs per proton based on energetic arguments.

The composition is also difficult to constrain in extragalactic jets. Circular polarization measurements indicate that the jets of the blazar 3C 279 are pair-dominated (Liodakis et al. 2021) and energetic arguments of the radio galaxy 3C 120 are consistent with a pair-dominated jet (Zdziarski et al. 2022b). Celotti & Fabian (1993), on the other hand, based on very-large baseline interferometry and spectral arguments for numerous sources, support an electron-proton plasma. The blazar TXS 0506+056, finally, due to the correlation with the high-energy neutrino IceCube-170922A, supports a baryon content in its jets as well (Aartsen et al. 2018).

Currently, the state-of-the-art to model jet launching and dynamics in a more a priori way are high-resolution simulations that solve the magneto hydrodynamic equations in the general relativistic regime (GRMHD). Such simulations have furthered our understanding of the accretion-launching paradigm and have shown that a Poynting flux dominated outflow can convert a significant amount of its initial magnetic energy into kinetic energy to accelerate the bulk flow (McKinney 2006; Komissarov et al. 2007, 2009; Tchekhovskoy, McKinney & Narayan 2008, 2009). The same simulations, have established that the accretion disc can significantly impact the spatial evolution of the jets not only at r_g-scale distances ($r_g = GM_{\rm bh}/c^2$, where $M_{\rm bh}$ is the mass of the black hole), but also further out. In particular, Chatterjee et al. (2019, hereafter CLTM19) performed a series of high-resolution GRMHD simulations of strongly magnetised systems to better understand the loading of jets with matter from the wind of the accretion disc. When the jets propagate in a medium, pinch instabilities can occur in the interface between the jet and the ambient medium to give rise to eddies that eventually allow for matter to entrain the jet (Eichler 1993; Spruit, Foglizzo & Stehle 1997; Begelman 1998; Giannios & Spruit 2006, CLTM19; Sironi, Rowan & Narayan 2021). Such mass entrainment can significantly affect the jet kinematics and hence the non-thermal emission.

Such GRMHD simulations, though, usually make the ideal gas assumption and therefore, cannot capture dissipative processes like particle acceleration self-consistently. Kinetic simulations of particles-in-cell (PIC), on the other hand, calculate the trajectories of individual particles based on first principles, allowing for a more detailed and comprehensive understanding of the relativistic outflows. Both GRMHD and PIC simulations, however, are very computational expensive, and they cannot easily be compared to observations through statistical methods that explore the full parameter phase space.

In this work, we develop a new treatment for incorporating mass-loading and thus evolving compositions in jets, and apply it to a multizone jet model. This treatment is inspired by recent GRMHD simulations such as CLTM19, to explore jet composition and its impact on the total jet power as well as its electromagnetic emission. In particular, we build on the multizone jet model developed by Markoff et al. (2005) that relies on the pioneering ideas of Blandford & Königl (1979), Hjellming & Johnston (1988), and Falcke & Biermann (1995). After many developments, the latest version of the model is `BHJet` (Lucchini et al. 2022), a multizone jet model that better connects the jet acceleration and jet physical quantities to the radiative output. For the first time, we connect the physically

Table 1. The definition of the jet quantities we use in this work with their units, some fiducial values (if applicable), the equation number where we define the parameter or whether it is a free parameter. See Sections 2 and 4 for further information.

Parameter	Units	Fiducial value(s)	Definition	Equation
z	r_g	–	distance from the black hole along the jet axis	–
z_0	r_g	6	distance of the jet base from the black hole	–
γ	–	$1-3$	bulk Lorentz factor of the flow	1
γ_0	–	1.1	bulk Lorentz factor at the jet base	–
r	r_g	–	cross-sectional radius of the flow	2
θ	rad	–	jet opening angle	3
n	cm^{-3}	–	jet (total) particle number density	4
n_0	cm^{-3}	–	jet number density at the jet base	16
n_e	cm^{-3}	–	jet pair number density	–
n_p	cm^{-3}	–	jet proton number density	–
ρ	$\mathrm{g\,cm}^{-3}$	–	jet mass density	7
ω	$\mathrm{erg\,cm}^{-3}$	–	total jet enthalpy	9
h	–	–	jet specific enthalpy	10
σ	–	–	magnetisation of the flow	13
σ_0	–	$1-100$	magnetisation of the flow at the jet base	19
μ	–	$1-100$	normalized total jet energy flux	18
$\langle\varepsilon_{\mathrm{e,\,p}}\rangle$	–	$1-100$	particle average Lorentz factor	25
z_acc	r_g	10^3	location where jet acceleration reaches the max value	free parameter
γ_acc	–	3	maximum Lorentz factor of the flow at z_acc	free parameter
r_0	r_g	$10-10^2$	jet base radius	free parameter
L_jet	L_Edd	0.002–0.02	injected jet power at the jet base	free parameter
η_e	–	$1-10^6$	jet pair-to-proton content	free parameter
σ_acc	–	0.1	magnetisation of the flow at the acceleration region	free parameter
k_BT_e	keV	–	electron peak energy at the jet base	free parameter

motivated model `BHJet` with hadronic acceleration, accounting for self-consistent energy conservation. We further present `HadJet`, a multizone, lepto-hadronic, mass-loaded jet model. In this work, we discuss the main physical properties of both models, and how `HadJet` can be used to address the jet-power crisis of lepto-hadronic models.

The paper is structured as follows. In Section 2, we describe the semi-analytical calculations for the magnetically accelerated jet accounting for both leptonic and hadronic acceleration and radiative processes. We present the results of the above jet model in Section 3. In Section 4, we describe the details of the mass-loaded jet model (`HadJet`) and present the results in Section 5. Finally, in Section 6, we discuss the implication of our new models on the proton power issue and conclude in Section 7.

2 MAGNETICALLY ACCELERATED STEADY-STATE JETS

We assume two initially cold, Poynting flux dominated jets of either leptonic or lepto-hadronic content that accelerate up to some maximum velocity because of magnetic energy dissipation (Vlahakis & Konigl 2003; McKinney 2006; Komissarov et al. 2007). At the region where the bulk velocity reaches the maximum value (acceleration region henceforth, denoted by z_acc), we further assume that energy is also dissipated to accelerate particles to non-thermal energies (Blandford & Rees 1974; Begelman, Blandford & Rees 1984). With our formalism, we cannot capture whether the magnetic energy dissipates immediately to particle acceleration (as in the case of magnetic reconnection) or if magnetic energy dissipates to kinetic energy first and this extra kinetic energy dissipates to particle acceleration through shocks (Bogovalov & Tsinganos 2005). We assume instead that the total energy of the jet is conserved at the particle acceleration region. From this point outwards along the jets, we assume a constant particle acceleration rate and discuss below how this assumption affects the evolution of both the jet velocity and magnetic field. In Table 1, we define all the parameters and their fiducial values (if applicable) that we use in this section.

2.1 Jet dynamical properties

Based on both semi-analytical and numerical calculations, the bulk jet Lorentz factor γ is expected to scale approximately as $z^{1/2}$, where z is the distance along the jet (Beskin & Nokhrina 2006; McKinney 2006). We parametrize the jet Lorentz factor as Lucchini et al. (2018) (and see also Potter & Cotter 2012)

$$\gamma(z \leq z_\mathrm{acc}) = \gamma_0 + (\gamma_\mathrm{acc} - \gamma_0)\frac{z^{1/2} - z_0^{1/2}}{z_\mathrm{acc}^{1/2} - z_0^{1/2}}, \quad (1)$$

where γ_0 is the initial Lorentz factor at the jet base and z_0 is the distance of the jet base from the black hole and γ_acc is the maximum bulk Lorentz factor at z_diss. We assume that the jets launch initially with the speed of sound, which for a relativistic flow with adiabatic index 4/3 is equal to 0.43 c, or $\gamma_0 = 1.11$ (Crumley et al. 2017).

The jets are thus set to be initially parabolic while they accelerate and become conical when they achieve γ_acc (Komissarov et al. 2009). We express the cross-sectional radius of the jet along the jet axis as

$$r = r_0 + (z - z_0)\tan(\theta), \quad (2)$$

where r_0 is the radius of the jet base and θ is the opening angle of the jets. Based on very long baseline interferometry observations and the Monitoring of jets in AGN with VLBA Experiments (MOJAVE; Pushkarev et al. see, e.g. 2009, 2017, we set the jet opening angle to be

$$\theta = \frac{0.15}{\gamma}. \quad (3)$$

While the number of particles along the jet is conserved, we express the number density of leptons as

$$n = n_0 \left(\frac{\gamma\beta}{\gamma_0\beta_0}\right)^{-1} \left(\frac{r}{r_0}\right)^{-2}, \quad (4)$$

where β is the jet velocity normalized to the speed of light and n_0 is the initial number density. We calculate n_0 by the power $L_{\rm jet}$ injected at the jet base in the comoving frame

$$L_{\rm jet} = 2\beta_0\gamma_0 {\rm c}\pi r_0^2\omega_0, \quad (5)$$

where we account for two identical jets (hence the factor of 2), and n_0 depends on $L_{\rm jet}$ and the initial conditions of the jet base as written out below. We write the jet enthalpy ω as (Falcke & Biermann 1995; Crumley et al. 2017)

$$\omega = \rho {\rm c}^2 + U_j + P_j = \rho c^2 + U_{\rm p} + P_{\rm p} + U_{\rm e} + P_{\rm e} + U_B + P_B, \quad (6)$$

where $U_j = U_{\rm p} + U_{\rm e} + U_B$ is the total internal jet energy density and $P_j = P_{\rm p} + P_{\rm e} + P_B$ is the total jet pressure. In the above equation, ρ is the jet mass density

$$\rho = n_{\rm p}\,{\rm m_p} + n_{\rm e}\,{\rm m_e}. \quad (7)$$

We express the number of protons in terms of the number of leptons as $n_{\rm p} = n_{\rm e}/\eta_e$, where $n_{\rm e/p}$ is the number density of leptons/protons, respectively, and $\eta_e \geq 1$ is a free parameter that remains constant unless the jets are mass-loaded (see below).

For an ideal gas, we can write the pressure terms as

$$P_{\rm e,p} = (\Gamma_{\rm e,p} - 1)\, U_{\rm e,p}, \quad (8)$$

where $\Gamma_{\rm e,p}$ is the adiabatic index. For the rest of the paper, we assume a relativistic pair content ($\Gamma_{\rm e} = 4/3$) at the jet base and a cold proton population ($\Gamma_{\rm p} = 5/3$) until the particle acceleration region (see below). For the pair temperatures, we are interested in this work, the flow remains cold even if it is dominated by pairs at the base. For $U_B = P_B = B^2/8\pi$, we write the jet enthalpy as

$$\omega = \rho {\rm c}^2 + \Gamma_{\rm p} U_{\rm p} + \Gamma_{\rm e} U_{\rm e} + \frac{B^2}{4\pi}. \quad (9)$$

We define the specific enthalpy of the gas as

$$h = \frac{U_g + P_g}{\rho {\rm c}^2} = \frac{\Gamma_{\rm p} U_{\rm p} + \Gamma_{\rm e} U_{\rm e}}{\rho {\rm c}^2}, \quad (10)$$

where we used equation (8). We calculate $U_{\rm e,p}$ by computing the integral

$$U_{\rm e,p} = \int \frac{dn_{\rm e,p}}{d\varepsilon_{\rm e,p}} \varepsilon_{\rm e,p} {\rm m_{e,p}} {\rm c}^2 {\rm d}\varepsilon_{\rm e,p}, \quad (11)$$

where $\varepsilon_{\rm e,p}$ is the Lorentz factor of the particles, but we can also express the internal energy density in terms of the average total energy of the particles

$$U_{\rm e,p} \simeq (\langle\varepsilon_{\rm e,p}\rangle - 1)\, n_{\rm e,p} {\rm m_{e,p}} {\rm c}^2, \quad (12)$$

where $\langle\varepsilon_{\rm e,p}\rangle$ is the average Lorentz factor of the pairs/protons of the jet segment (see below for calculation). This equation is more convenient than equation (11) for the following discussion, however, we note that it might not be accurate enough if a significant fraction of the leptons accelerate to non-thermal energies, in particular in a hard power law with slope <2.

A useful parameter to characterize the jets is the magnetisation. We define the magnetisation of a flow as the Poynting flux over the total energy flux (Nokhrina et al. 2015)

$$\sigma = \frac{B^2}{4\pi(\rho {\rm c}^2 + {\rm U_g} + {\rm P_g})} \Rightarrow$$

$$\sigma = \frac{B^2}{4\pi\rho {\rm c}^2 (1+h)}. \quad (13)$$

When the flow is cold ($h \ll 1$), the above definition reduces to the well-known expression of

$$\sigma_c \simeq \frac{B^2}{4\pi\rho {\rm c}^2}. \quad (14)$$

We write the enthalpy of equation (9) of a flow from equations (10) and (13) as

$$\omega = \rho {\rm c}^2 (1+\sigma)(1+h). \quad (15)$$

We can plug this equation into equation (5) to calculate the particle number density at the jet base

$$n_0 = \frac{L_{\rm jet}}{2\beta_0\gamma_0 c\pi r_0^2\,({\rm m_p}/\eta_e + {\rm m_e}) c^2 (1+\sigma_{\rm c})}. \quad (16)$$

We further use the relativistic Bernoulli's equation to express the conservation of energy flux along the jet axis (Königl 1980)

$$\gamma\frac{\omega}{\rho} = \text{constant}, \quad (17)$$

and from equation (15), we rewrite the above equation such as to define:

$$\mu \equiv \gamma\,(1+\sigma)(1+h), \quad (18)$$

where μ is the normalized total energy flux and is conserved along the jets (unless the jets entrain mass; see below). In a cold jet where the specific enthalpy h is negligible, equation (18) simplifies to $\mu \simeq \gamma\,(1+\sigma_c)$. This is a very well-known equation to express the maximum jet Lorentz factor when the majority of the Poynting flux has been converted to kinetic energy ($\gamma_{\rm max} \simeq \mu$). In this work, we keep this term in our calculations because h is an estimate of the energy that the accelerated particles carry in each jet segment, and in numerous instances can dominate both the magnetisation and the jet Lorentz factor.

While the jets accelerate between the launching point and the acceleration region $z_{\rm acc}$, μ remains constant. We write equation (18) at the jet base and equate it to the acceleration region and solve for the initial magnetisation

$$\gamma_0(1+\sigma_0)(1+h_0) = \gamma_{\rm acc}(1+\sigma_{\rm acc})(1+h_{\rm acc}) \Rightarrow$$

$$\sigma_0 = \frac{\gamma_{\rm acc}}{\gamma_0}(1+\sigma_{\rm acc})\left(\frac{1+h_{\rm acc}}{1+h_0}\right) - 1, \quad (19)$$

and in general for every z below the acceleration region

$$\sigma(z \leq z_{\rm acc}) = \frac{\gamma_0}{\gamma}(1+\sigma_0)\left(\frac{1+h_0}{1+h}\right) - 1, \quad (20)$$

or

$$\sigma(z \leq z_{\rm acc}) = \frac{\gamma_{\rm acc}}{\gamma}(1+\sigma_{\rm acc})\left(\frac{1+h_{\rm acc}}{1+h}\right) - 1. \quad (21)$$

With the magnetisation and the specific enthalpy at the acceleration region as free parameters ($\sigma_{\rm acc}$ and $h_{\rm acc}$, respectively), we set the initial magnetisation σ_0 required for the flow to be Poynting flux dominated and to carry enough energy to efficiently accelerate particles to non-thermal energies. In particular, we use $\sigma_{\rm acc}$ as a free parameter because this is the simplest way to force our semi-analytical model to have dissipated the majority of the magnetisation

at the acceleration region, and we set $h_{\rm acc}$ from equation (10) (see also the discussion on particle acceleration below). The initial specific enthalpy h_0 is set by the free parameters at the jet base, and as we discuss below, it is negligible for the standard case of an initially cold jet that we study here (see Section 3.1).

Above the acceleration region, we assume the toroidal component dominates the poloidal component of the magnetic fields similar to Blandford & Königl (1979), so

$$B(z > z_{\rm acc}) = B_{\rm acc}\left(\frac{z}{z_{\rm acc}}\right)^{-1}, \tag{22}$$

where $B_{\rm acc}$ is the magnetic field strength at the acceleration region.

Based on equation (13), we generalize the expression of σ for every z above the acceleration region

$$\sigma(z \geq z_{\rm acc}) = \sigma_{\rm acc}\frac{\rho_{\rm acc}(1+h_{\rm acc})}{\rho(1+h)}\left(\frac{z}{z_{\rm acc}}\right)^{-2}. \tag{23}$$

2.2 The acceleration region and particle acceleration

We assume that the pairs at the jet base follow a Maxwell–Jüttner distribution (MJ; the relativistic regime of the Maxwell–Boltzmann distribution) with a peak energy $k_{\rm B}T_{\rm e}$ that is a free parameter. The population of protons on the other hand is cold, making the flow cold at the launching point.

By the time the flow reaches the acceleration region, the Poynting flux dominated flow has dissipated the magnetic energy, hence the magnetisation has dropped to a value $\sigma_{\rm acc}$. At the same region, we assume a constant fraction $f_{\rm pl} \sim 0.1$ of particles accelerates to a non-thermal power law between a minimum and a maximum energy. For the leptonic scenario, we assume that only pairs accelerate in a power law from an energy $\varepsilon_{\rm min}{\rm m_e c^2} = k_{\rm B}T_{\rm e}$ to some $\varepsilon_{\rm max}$ that we calculate self-consistently by equating the acceleration time-scale $4\varepsilon {\rm m_e c^2}/(3f_{\rm sc}ecB)$ to the escape time-scale (Jokipii 1987; Aharonian 2004). The acceleration efficiency $f_{\rm sc}$ depends on the particle acceleration mechanism, but we fix it at a value between 0.01 and 0.1 leading to a maximum electron energy of the order of GeV for the case of a BHXB. For the lepto-hadronic scenario, we assume that protons accelerate as well in a power law from an $\varepsilon_{\rm min} = 1$ to some $\varepsilon_{\rm max}$ that we calculate by equating the acceleration time-scale to the (lateral) escape time-scale $r/{\rm c}$ of the jet segment and for the case of BHXBs, it may attain values of the order of 100 TeV and above (Pepe, Vila & Romero 2015; Kantzas et al. 2021, 2022). We constrain the non-thermal particle distributions by assuming that they extend up to the maximum energy, and then they drop exponentially

$$\frac{{\rm d}n\,(\varepsilon)}{{\rm d}\varepsilon} = K\varepsilon^{-p}\,\exp\left(-\varepsilon/\varepsilon_{\rm max}\right), \tag{24}$$

where n is the particle number density for any species, K is the normalization, and the slope p of the power law depends on the particle acceleration mechanism, but we use it as a free parameter between 1.7 and 2.4, assuming it remains the same between electrons and protons.

Finally, we derive the average Lorentz factor for every species from the equation

$$\langle\varepsilon\rangle = \frac{\int \varepsilon\frac{{\rm d}n}{{\rm d}\varepsilon}{\rm d}\varepsilon}{\int \frac{{\rm d}n}{{\rm d}\varepsilon}{\rm d}\varepsilon}. \tag{25}$$

2.3 Jet evolution and particle acceleration

Beyond the acceleration region where particles accelerate to non-thermal energies as well, the specific enthalpy can become important because the average Lorentz factors of pairs and/or protons may have significantly increased (see equation 10). We write the bulk Lorentz factor for every jet segment above the acceleration region for an outflow from equation (18):

$$\gamma(z) = \gamma_{\rm acc}\left(\frac{1+h_{\rm acc}}{1+h}\right)\left(\frac{1+\sigma_{\rm acc}}{1+\sigma}\right). \tag{26}$$

2.4 Radiative processes

We suggest the interested readers to seek for further details on the radiative processes in Lucchini et al. (2022) for the leptonic processes, and in Kantzas et al. (2021) for the hadronic processes. We nevertheless briefly discuss the main processes here for completeness.

2.4.1 Leptonic processes

The main three radiative processes of leptonic nature that we require in our analysis here are: synchrotron radiation, ICS and pair production. In particular, the thermal pairs of the MJ distribution and the non-thermal power-law tail above the dissipation region, lose energy due to cyclo-synchrotron radiation (Blumenthal & Gould 1970; Rybicki & Lightman 2008). We only account for the average magnetic field strength of the particular jet segment and assume an isotropic distribution of pitch angles that we average over.

We further account for the ICS between the pairs and the radiation fields of the outflow (Blumenthal & Gould 1970; Rybicki & Lightman 2008). In particular, in this work, we neglect any external photon field and only allow for ICS between the emitting pairs and the synchrotron photons (synchrotron self Compton; SSC). Plausible external photon fields may be important in the case of AGN jets but for the study-cases as BHXBs we discuss in this work, we have shown in previous works that the external photon fields are not critical (see e.g. Kantzas et al. 2021; Lucchini et al. 2021, however, see also Zdziarski et al. 2014 and Zacharias et al. 2022 for cases where the external photon fields may be important to explain the γ-ray spectrum). For simplicity, we also neglect any accretion disc in the following discussion, but we do account for it when examining particular sources, following Lucchini et al. (2022). For the ICS processes, we account for the Klein–Nishina regime when necessary, and allow for multiple scatterings to better capture the evolution of the exponential cut off. This particular process is the most computationally expensive amongst the leptonic ones, we hence choose to neglect it when the radiative output becomes 10^4 times smaller than the synchrotron counterpart for the particular segment.

The final process of leptonic nature we account for is the photon annihilation to pair production and the annihilation of an electron/positron pair to two photons (Coppi & Blandford 1990). These two processes are usually negligible, so we do not mention them unless we discuss their impact on the particle population or the spectrum (see e.g. Connors et al. 2019).

2.4.2 Hadronic processes

We account for both proton–proton (pp) and proton–photon (pγ) processes when accelerated protons interact with the cold protons of

the flow and the jet radiation, respectively. In particular, we use the semi-analytical parametrization of Kelner, Aharonian & Bugayov (2006) for the pp interactions, and Kelner & Aharonian (2008) for the pγ. The above analysis provides the resulted distributions of secondary particles (pions that decay into muons, and the muons decay into neutrinos, pairs and γ-rays) and hence, cannot account for any synchrotron radiation of muons and/or pions, but for the current systems we examine, we see that it is not required. We do however consider the cyclo-synchrotron radiation of secondary pairs due to the presence of the magnetic field.

In our particular analysis, we find that the synchrotron photons produced by the primary pairs act as the target for the pγ interactions. Based on this analysis, we can also produce the neutrino counterpart in a self-consistent manner (Kantzas et al. in prep).

3 RESULTS FOR THE STEADY-STATE JETS

We first present the results of the analysis of the model where we do not account yet for any mass entrainment. In this flavour of the model, we try to better understand and constrain the number of leptons in the jets with respect to the number of protons η_e. We further present the jet dynamical properties and their corresponding multiwavelength spectra before we compare them to ones when we account for mass-loading.

3.1 Specific enthalpy and particle acceleration

We can express equation (10) as

$$h = \frac{\Gamma_{\rm e}(\langle\varepsilon_{\rm e}\rangle - 1) + \Gamma_{\rm p}(\langle\varepsilon_{\rm p}\rangle - 1)\dfrac{{\rm m_p}/{\rm m_e}}{\eta_e}}{1 + \dfrac{{\rm m_p}/{\rm m_e}}{\eta_e}}, \tag{27}$$

where we used equations (7), (12), and $n_{\rm p} = n_{\rm e}/\eta_e$.

From the above equation, we see that the specific enthalpy depends merely on the ratio between pairs and protons. Moreover, we see that h strongly depends on any mechanism (acceleration or cooling) that would significantly change the average Lorentz factor of the particles.

In Fig. 1, we plot the specific enthalpy h as a function of the pair-to-proton ratio η_e for various values of $\langle\varepsilon_{\rm e}\rangle$ and $\langle\varepsilon_{\rm p}\rangle$. Both $\langle\varepsilon_{\rm e}\rangle$ and $\langle\varepsilon_{\rm p}\rangle$ depend on the power law slope of the accelerated particles, as well as the minimum and the maximum particle energy. We let η_e to scale between a few and 10^6 although the latter values are extreme and perhaps not physically expected. A jet with more protons than leptons ($\eta_e < 1$) would be positively charged and hence is unphysical. On the other hand, a very large number of pairs per protons would be difficult to explain the observed Lorentz factors on parsec scales (Ghisellini & Tavecchio 2010). In all panels, the vertical line corresponds to $\eta_e = {\rm m_p}/{\rm m_e}$, which roughly indicates the transition from a pair dominated jet ($\eta_e \gtrsim {\rm m_p}/{\rm m_e}$) to a jet of equal number of protons and leptons ($\eta_e \lesssim {\rm m_p}/{\rm m_e}$).

In the top left plot of Fig. 1 where no protons accelerate at all, and in particular in the case of approximately equal amount of pairs and protons ($\eta_e \sim 1$), we see that the specific enthalpy is significantly smaller than unity ($h \ll 1$). This is in agreement with the initial set ups of GRMHD simulations where the specific enthalpy is usually neglected (McKinney 2006; Komissarov et al. 2007). In the other regime, where the flow is dominated by pairs ($\eta_e \gtrsim 10^3$), we see that $h \sim \Gamma_e\langle\varepsilon_{\rm e}\rangle$ (equation 27). In the top right plot of Fig. 1, where we assume $\varepsilon_{\rm e,\,min} = 10$, we see a similar evolution of η_e. The main difference is that $\langle\varepsilon_{\rm e}\rangle$ goes to larger values, hence h goes to larger values as well. From both plots, we see that for a purely leptonic flow, the specific enthalpy is not negligible and in fact, it can be as important as the magnetisation and the kinetic energy in the evolution of the jets (as discussed below).

In the middle plots of Fig. 1, where protons accelerate in a similar power law as the accelerated pairs, we see a significantly different evolution of h for different jet content. In particular, in the case where $\varepsilon_{\rm e,\,min} = 1$ and $\varepsilon_{\rm p,\,min} = 1$ (middle left plot), we see that for an equal pair-to-proton jet content ($\eta_e = 1$), h is driven by the accelerated protons, and in fact, $h \sim \Gamma_p\langle\varepsilon_{\rm p}\rangle$ (see equation 27). In the regime of a purely leptonic flow ($\eta_e \gg 1$), we see that $h \sim \Gamma_e\langle\varepsilon_{\rm e}\rangle$ and depending on whether $\langle\varepsilon_{\rm e}\rangle > \langle\varepsilon_{\rm p}\rangle$ or $\langle\varepsilon_{\rm e}\rangle < \langle\varepsilon_{\rm p}\rangle$, h will increase or decrease, respectively. In the right-hand side of the middle panels of Fig. 1, we get larger values of $\langle\varepsilon_{\rm e}\rangle$ because of the larger value of $\varepsilon_{\rm e,\,min}$ (for the particular $p = 2.2$), and hence the specific enthalpy may attain significantly larger values reaching values of the order of $\Gamma_e\langle\varepsilon_{\rm e}\rangle$.

In the bottom plots of Fig. 1 where protons accelerate in a power law from a $\varepsilon_{\rm p,\,min} = 10$, we see that a flow of $\eta_e \sim 1$ has a significant fraction of energy in the specific enthalpy because $h \sim \Gamma_p\langle\varepsilon_{\rm p}\rangle \sim 90$. In the purely leptonic regime ($\eta_e \gg 1$), we see that h can drop to values smaller than 10 depending on the average Lorentz factor of the pairs. In the case where pairs accelerate in a power law from a high energy as $10\,{\rm m_e c^2}$ (right-hand side plot of lowermost panels of Fig. 1), the energy content in the specific enthalpy remains significant for both $\eta_e \sim 1$ and $\eta_e \sim 10^6$.

From Fig. 1, we overall see that the specific enthalpy of a flow that accelerates particles can be important in the evolution of the flow (see also discussion below). In the case where only pairs accelerate in the jets and for an equal amount of electrons-to-protons as is commonly assumed in GRMHD (left-hand side of the uppermost panels, and in particular in the case of one), we see that the specific enthalpy is indeed negligible ($h \ll 1$). In any other case where both pairs and protons accelerate in the jets, and regardless of the jet content (either pair-dominated or equal pair-to-proton content), the specific enthalpy of the flow might be of the order of a few-to-tens, and hence it is important for the evolution of the flow (see also discussion of CLTM19).

In the Appendix A, we discuss the evolution of h in the case of a hard power law of accelerated particles with $p = 1.7$ power law index. Such hard values, resulting from efficient particle acceleration e.g. in magnetic reconnecting regions (Sironi, Petropoulou & Giannios 2015; Ball, Sironi & Özel 2018) or relativistic shocks (see e.g. Böttcher & Baring 2019), lead to even larger values of h of the order of thousands. Such large values of h along with large bulk Lorentz factors as observed in relativistic outflows in AGN and GRBs, would lead to significantly larger values of total energy flux μ compared to those in the literature (Komissarov et al. 2007, 2009; Petropoulou, Psarras & Giannios 2022). Furthermore, equation (18), which has broadly been used to provide an estimate for the maximum bulk Lorentz factor when the magnetic energy has been converted into kinetic energy, would not hold anymore and a more careful treatment where the specific enthalpy is calculated from first principles is needed.

3.2 Total energy flux evolution for steady state jets

In Fig. 2, we plot the evolution of μ along the jets with the different components: magnetisation (σ), bulk Lorentz factor (γ), and specific enthalpy (h). In the left plots of Fig. 2, we assume a jet content of equal number of leptons and protons ($\eta_e = 1$) and in the right plots, we assume a pair-dominated outflow ($\eta_e = 10000$). In the top panels, we assume that only leptons accelerate to non-thermal energies, whereas

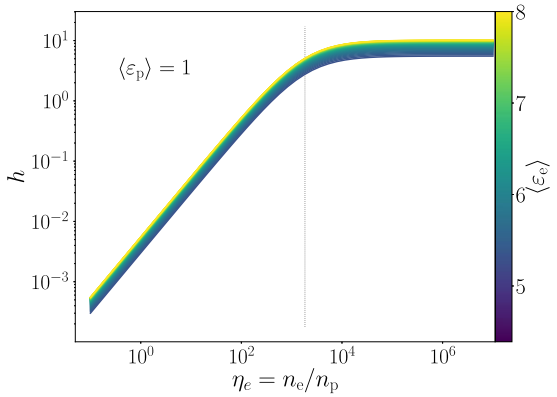

(a) Purely leptonic acceleration with $\varepsilon_{e,min} = 1.5$.

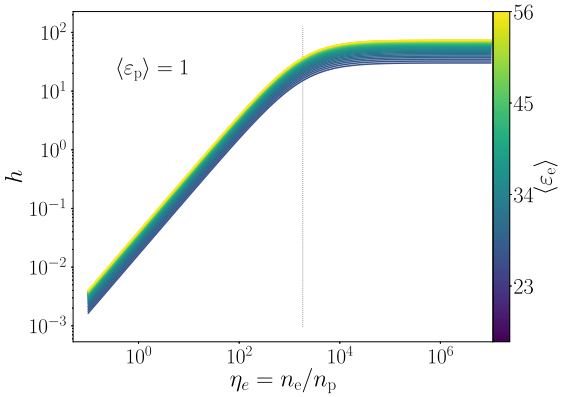

(b) Purely leptonic acceleration with $\varepsilon_{e,min} = 10$.

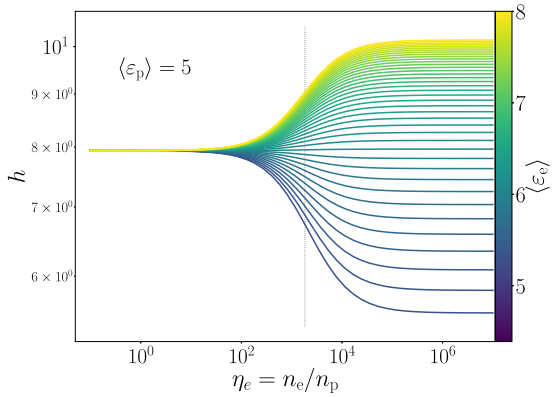

(c) Leptohadronic acceleration with $\varepsilon_{e,min} = 1.5$.

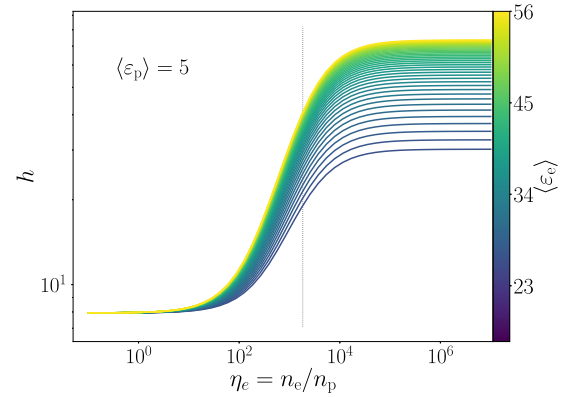

(d) Leptohadronic acceleration with $\varepsilon_{e,min} = 10$.

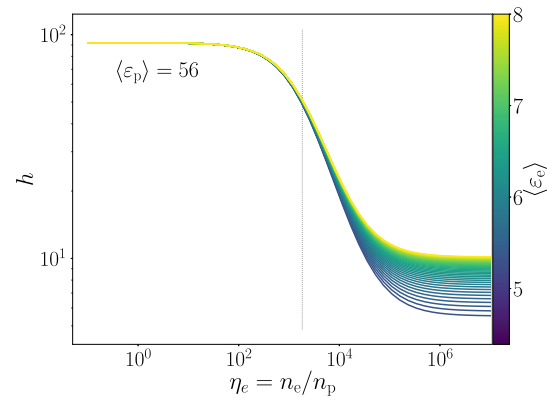

(e) More efficient hadronic, and leptonic acceleration with $\varepsilon_{e,min} = 1.5$.

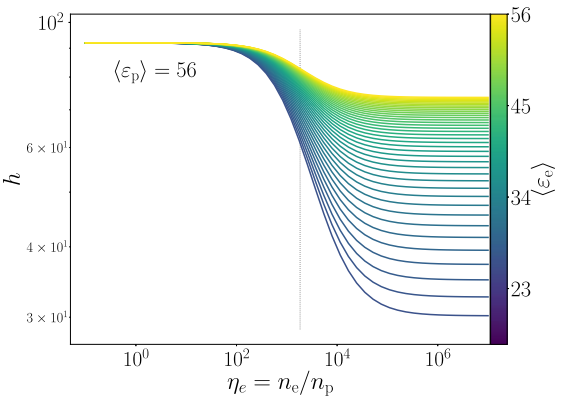

(f) More efficient hadronic, and leptonic acceleration with $\varepsilon_{e,min} = 10$.

Figure 1. The jet specific enthalpy h as a function of the jet content $\eta_e = n_e/n_p$. In all plots, we assume a soft non-thermal power law with $p = 2.2$ to derive the average particle Lorentz factors from equation (25). The colour-map corresponds to the average Lorentz factor of electrons, with lighter colours to indicate more efficient acceleration. In the *left* column and for a less efficient electron acceleration, the minimum Lorentz factor of the pairs is $\varepsilon_{e,\,min} = 1.5$, whereas in the *right* column with a more efficient electron acceleration, $\varepsilon_{e,\,min} = 10$. In the *top* panels, we assume only leptonic acceleration, in the *middle*, we assume non-efficient hadronic acceleration with $\varepsilon_{p,\,min} = 1$ and $\varepsilon_{p,\,max} = 100$, and in the *bottom* panels, we assume efficient hadronic acceleration with $\varepsilon_{p,\,min} = 10$ and $\varepsilon_{p,\,max} = 10^7$. The vertical lines correspond to $\eta_e = m_p/m_e$.

in the bottom panels, we assume that hadrons accelerate as well in a power law with the same index.

In the top left panel, where we account only for leptonic acceleration with $\langle \varepsilon_e \rangle = 6$, we see that the initial magnetisation of the outflow converts to bulk kinetic energy whereas the magnetisation drops to $\sigma_{acc} = 0.1$ (a free parameter). The specific enthalpy starts as negligible at the cold jet base ($h_0 \ll 10^{-2}$) and remains insignificant for the jet evolution above the particle acceleration region z_{acc}. This particular regime where the specific enthalpy is insignificant and the jet composition is one lepton per proton, is the regime considered by

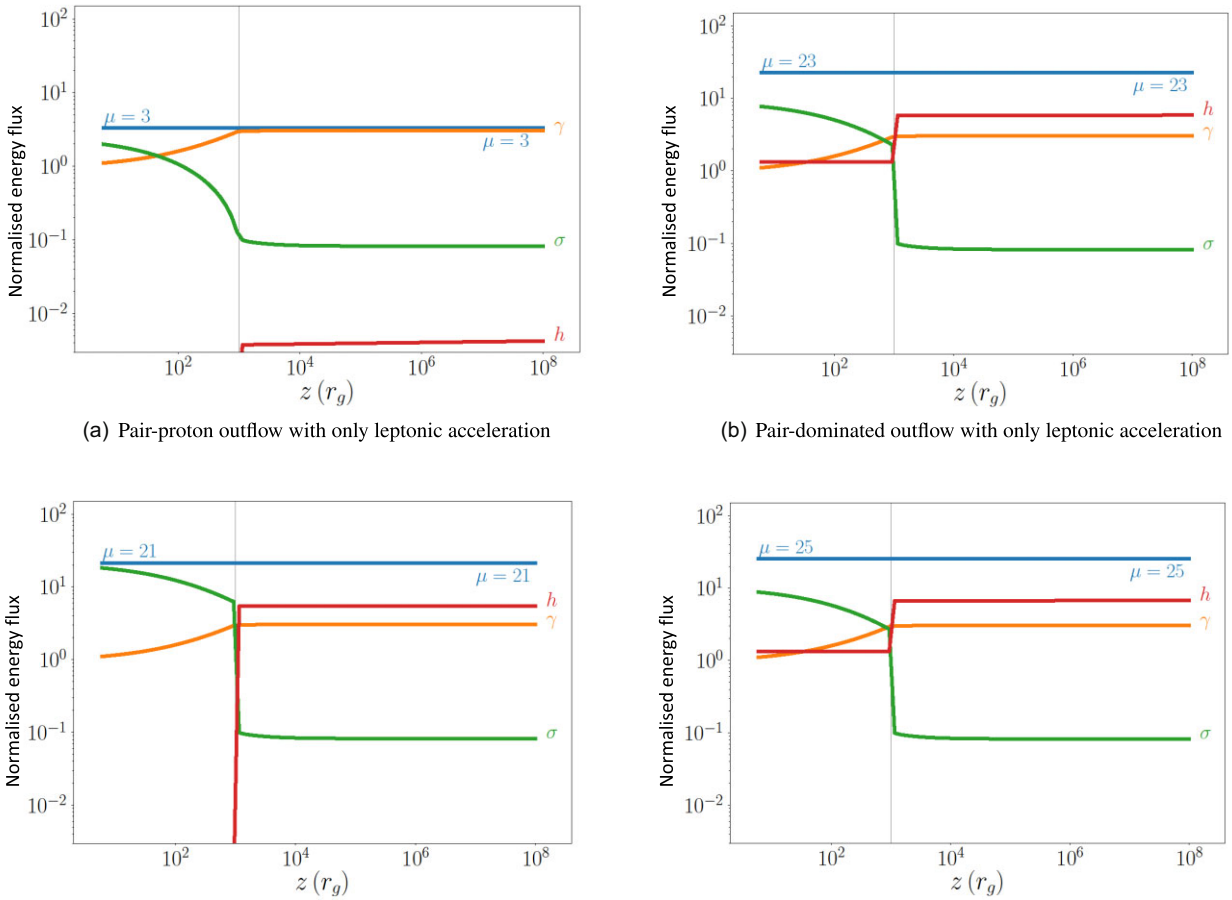

(a) Pair-proton outflow with only leptonic acceleration

(b) Pair-dominated outflow with only leptonic acceleration

(c) Pair-proton outflow with lepto-hadronic acceleration

(d) Pair-dominated outflow with lepto-hadronic acceleration

Figure 2. The energy jet components γ (the bulk Lorentz factor), σ (the magnetisation), and h (the specific enthalpy) that follow the relation $\mu = \gamma(1+\sigma)(1+h)$ (equation 18). In all plots, we use $z_0 = 6\,r_g$, $z_{\rm acc} = 10^3\,r_g$, $\gamma_{\rm acc} = 3$, $\sigma_{\rm acc} = 0.1$, and $\langle\varepsilon_{\rm e}\rangle = 6$ (see Table 1 for definitions). We show a pair/proton flow with $\eta_e = 1$ in the *left* column and a pair-dominated flow with $\eta_e = 10000$ in the *right* column. In the *top* panels, we only account for leptonic acceleration and in the *bottom* panels, we consider hadronic acceleration as well with $\langle\varepsilon_{\rm p}\rangle = 4$.

most GRMHD simulations (see also Section 4), and in fact, is the only regime that `BHJet` can probe self-consistently so far (Lucchini et al. 2022). With the current improvement of this work, we can now further explore the jet kinematics to other regimes where the distribution of the internal energy density is important in the evolution of the jet dynamics and the electromagnetic spectrum.

In the top right panel, where we assume a pair-dominated jet ($\eta_e \gg 1$) that accelerates only leptons, we see that the initial magnetisation converts almost equally to bulk kinetic energy and internal energy (h is now comparable to γ). The initial specific enthalpy at the jet base is larger compared to the previous case, and based on equation (18), we see that also μ has significantly increased (see also Section 3.1).

In the bottom left panel of Fig. 2, where we account for hadronic acceleration with $\langle\varepsilon_{\rm p}\rangle = 4$, we see that the initial magnetisation dissipates almost equally to kinetic and internal energy. The initial specific enthalpy is negligible at the cold jet base, but when particles accelerate at the acceleration region, h increases to values comparable to γ. Finally, in the bottom right panel, where the jet is pair-dominated, we see that the specific enthalpy at the jet base is of the order of 1 but still much smaller than the initial magnetisation.

In Fig. 2, according to the approach we follow here, h can overall be significant for the jet evolution depending on the hadronic acceleration and the jet content. The former, in particular, strongly depends on the jet properties, but we cannot capture this non-linear behaviour of the jet evolution, its effect on the particle acceleration and the consequent feedback of particle acceleration back to the jet evolution without significantly increasing the computational cost of the model. However, we can still investigate the jet properties to gain a better insight on jet physics.

In Appendix B, we present a more detailed series of jet evolution for various jet quantities and different average particle Lorentz factors. Overall, we find that for many physical scenarios, the specific enthalpy becomes important for the jet evolution, especially in the case where hadrons accelerate in the jets as well, and for pair-dominated outflows (see also Section 3.1).

3.3 Electromagnetic spectrum of steady state jets

We plot in Fig. 3 the multiwavelength spectra that correspond to the four different models of Fig. 2. In particular, in the top panels, we plot the purely leptonic scenarios, whereas in the bottom, we plot the lepto-hadronic models. For the left plots, we assume one proton per electron ($\eta_e = 1$), whereas on the right plot, we examine the extreme case of $\eta_e = 10^4$.

For all four panels, we assume a quite 'warm' MJ distribution of leptons with $k_B T_e = 1000\,{\rm keV}$, an initial jet-radius of $10\,r_g$ in which

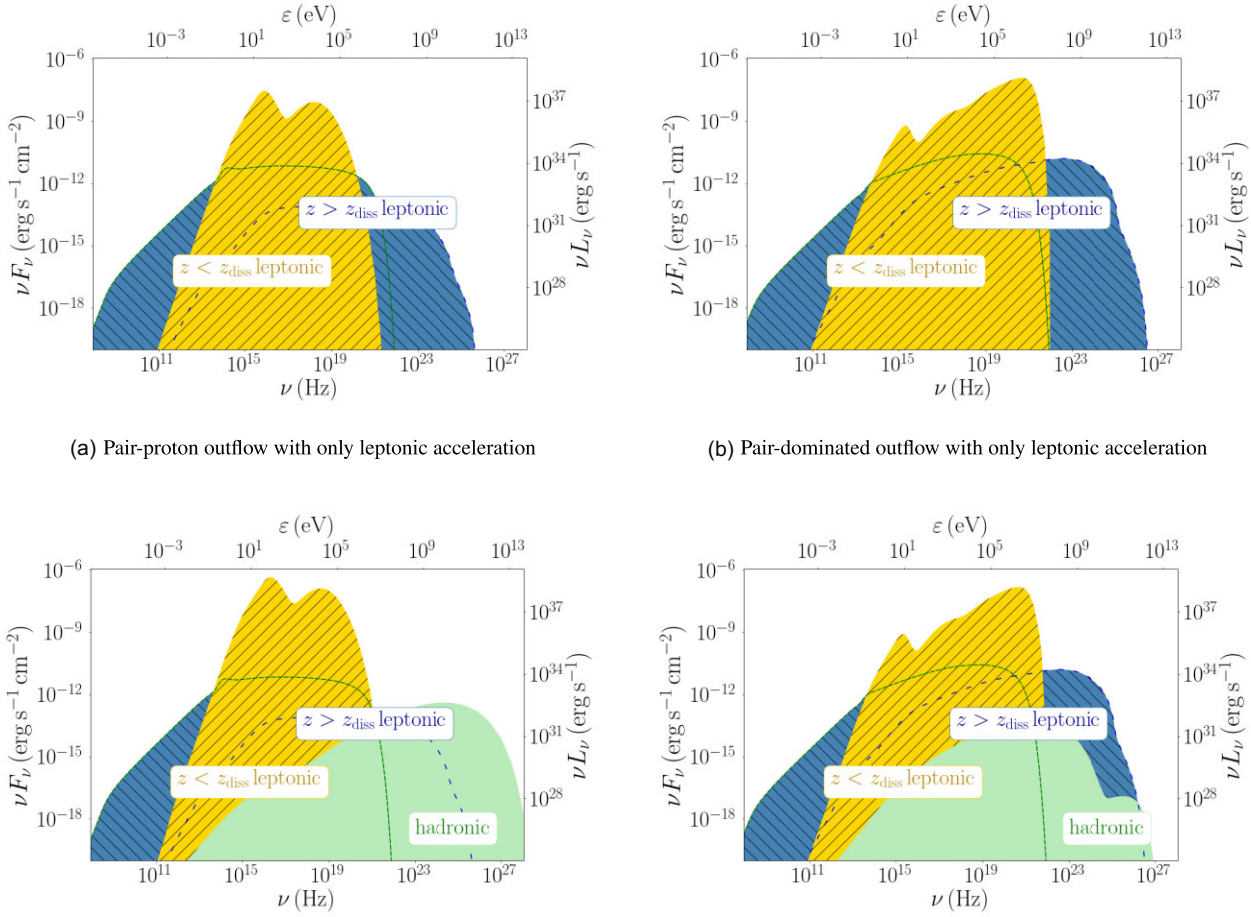

(a) Pair-proton outflow with only leptonic acceleration

(b) Pair-dominated outflow with only leptonic acceleration

(c) Pair-proton outflow with lepto-hadronic acceleration

(d) Pair-dominated outflow with lepto-hadronic acceleration

Figure 3. The predicted spectral energy distributions for the four models of Fig. 2. In the *top* panels, we only account for leptonic acceleration, and in the *bottom* ones, we consider both leptonic and hadronic. In the two *left* plots, we assume one proton per electron ($\eta_e = 1$), and in the *right* ones, we assume $\eta_e = 10^4$. In all four panels, we use $k_B T_e = 500\,\mathrm{keV}$, and $z_{\rm diss} = 1000\, r_g$ for a $10\,\mathrm{M}_\odot$ BHXB at 3 kpc. We also assume $L_{\rm jet} = 2 \times 10^{-2}\, L_{\rm Edd}$ for the leptonic scenarios and $L_{\rm jet} = 2 \times 10^{-3}\, L_{\rm Edd}$ for the hadronic. The aforementioned values lead to $\langle \varepsilon_{\rm e} \rangle = 5$. We highlight the contribution of the jet-segments before the dissipation region (yellow shaded) and that of the jet-segments above the dissipation region (blue shaded). We show the synchrotron emission with densely dashed green line, and the contribution of the ICS with loosely dashed blue line. Finally, the green shaded region is the hadronic contribution, where we include both neutral pion decay and the synchrotron radiation of the secondary electrons.

we inject some power equal to $10^{-2}\, L_{\rm Edd}$ for the leptonic models, and 10^{-3} for the lepto-hadronic ones. The particle acceleration that happens at $1000\, r_g$ leads to a power-law of particles with an index of 2.2. In all panels, we show the contribution to the spectrum of the jet segments before the dissipation region (yellow-shaded) and above (blue-shaded). For the lepto-hadronic model of the bottom panels, we include the hadronic contribution as green-shaded. Finally, the densely dashed line shows the synchrotron contribution, whereas the loosely dashed line corresponds to the ICS.

In the top left panel of Fig. 3, we see the emission from the thermal electrons dominates in the UV and X-ray bands, whereas the outer jets dominate in the radio bands via synchrotron radiation and in the GeV with ICS. In the case where we assume an increased ratio of pairs (top right panel), for the same initial conditions, we see once more the emission from the thermal pairs to dominate the UV/X-ray bands, but the X-ray luminosity is increased because the initial pair number density has increased (see equation 16).

In the lepto-hadronic cases of the bottom panels of Fig. 3, we see that the pair content may significantly affect the SED, and in particular the high-energy part. For the case of one proton per lepton, we see that the GeV-to-TeV spectrum first drops exponentially due to the synchrotron emission of the primary pairs, but later increases due to the hadronic contribution of the pγ interactions. The ICS contribution in this particular case is well below the hadronic contribution (loosely dashed line). In the pair-dominated jet of the right-hand panel, we see that the increased number of pairs leads to a stronger GeV-to-TeV flux that dominates over the hadronic contribution.

4 MASS LOADED JETS

High-resolution GRMHD simulations of accreting black holes that launch highly collimated jets suggest that a significant portion of the wind from the accretion disc might end up in the jet via entrainment. While the jets accelerate in a dense surrounding medium, they are subject to lateral pressure from the wind of the accretion disc that results in jet-wind collisions, causing the jet to wobble. Pinch instabilities form at the jet-wind interface close to the black hole,

almost independently of the initial magnetisation of the jet, as long as it starts out Poynting flux dominated. These instabilities dissipate magnetic energy to heat and increases the specific enthalpy of the jet (see e.g. Eichler 1993; Bowman, Leahy & Komissarov 1996; Spruit et al. 1997; Begelman 1998; Giannios & Spruit 2006; Bromberg & Tchekhovskoy 2015).

Interestingly, two properties of a collimated jet change at distances $\sim 10^2 - 10^3\, r_g$: (1) The toroidal component of the magnetic field starts to dominate over the poloidal component, and (2) the jet speed exceeds the local fast magnetosonic wave speed, i.e. becomes superfast, the magnetic analogue of the fluid becoming supersonic (CLTM19). Beyond this region, the jet becomes more susceptible to instabilities forming at the interface between the flow and the ambient medium. In particular, magnetic pinch instabilities lead to the formation of eddies that trap matter from the wind and drive it inwards through the jet-wind interface, allowing for mass entrainment (Mignone et al. 2013; Gourgouliatos & Komissarov 2018; Bodo et al. 2021). Without such eddies, significant mass entrainment into the jet from the external medium may not be possible due to the jet's strong magnetic field. Hence, we link the region where the mass-loading becomes important because of instabilities explicitly to the region where non-thermal particle acceleration occurs. Following the results of CLTM19, we connect this region to the first particle acceleration region of jets as originally proposed by (Markoff et al. 2005; Polko, Meier & Markoff 2014).

In this work, we parametrize the fiducial model B10 of CLTM19 to derive a semi-analytical formalism that connects the mass loading region to the particle acceleration region, and study its impact on the emitted electromagnetic spectrum by studying both the leptonic and the hadronic processes we discussed above. We consider B10 for our problem because the jet undergoes strong collimation out to very large scales. Other models explored in CLTM19 either have too small an accretion disc, such that there is hardly any lateral pressure from the disc wind. The jets therefore become uncollimated and thus conical within $1000\, r_g$, and hence do not properly represent the highly collimated, parabolic, large-scale jets we are targeting. Further, the fast lateral expansion of the uncollimated jet suppresses pinch instabilities (Moll, Spruit & Obergaulinger 2008; Granot, Komissarov & Spitkovsky 2011; Porth & Komissarov 2015) and thus exhibits little to no mass-loading (CLTM19).

CLTM19 confirm that the magnetic energy converts to kinetic energy, accelerating the jets similar to what was found in previous works (McKinney 2006; Komissarov et al. 2007, 2009). When matter is entrained by the jets, further magnetic energy is dissipated to heat up the jet, and the inertia of the entrained gas slows down the jet. The mass entrainment leads to a decrease of the total (specific) energy flux μ along the jets up to the distance where the mass loading stops. Beyond distances of a few $10^4\, r_g$, the CLTM19 jet properties have not achieved steady-state as the slow, mass-loaded jet is still punching through the ambient medium at this point of time in the GRMHD simulation. Indeed, the simulations suggest that as the jet slowdown due to mass loading suppresses pinch instabilities further along the jet, and therefore, mass loading becomes considerably weaker beyond $10^4\, r_g$. As a result, when the simulated jets attain steady-state out to $\gtrsim 10^5\, r_g$, we expect that μ should be conserved for the rest of the jets and there would be jet re-acceleration while both the magnetisation and the specific enthalpy decrease.

Inspired by the simulation results, our semi-analytical 'mass-loaded' jet model assumes that the mass loading initiates at a distance $z_{\rm diss} \sim 100\, r_g$ and ends at $100\, z_{\rm diss}$, with a net increase of $f_\rho = 10$ in the jet mass density. Beyond $100\, z_{\rm diss}$, we assume a constant μ and steady jet acceleration. In Fig. 4, we plot the mass density of a mass loaded jet (solid line) and compare it to a non-loaded steady state jet, assuming one proton per lepton. We show the resulting energy components (γ, σ, and h) of the B10 model of CLTM19 in Fig. 5 with dashed lines, and below, we discuss the way we parametrize these quantities.

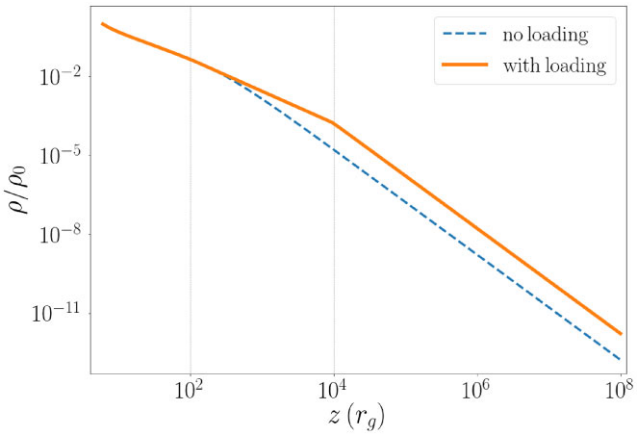

Figure 4. The mass density profile of a mass loaded jet (solid line) compared to a steady state jet without mass loading (dashed line). Both profiles are normalized to the initial mass density at the jet base. The mass loading initiates at a distance $z_{\rm diss}$ and at $100\, z_{\rm diss}$ the mass density has increased by a factor of 10 compared to a non-loading, steady-state jet.

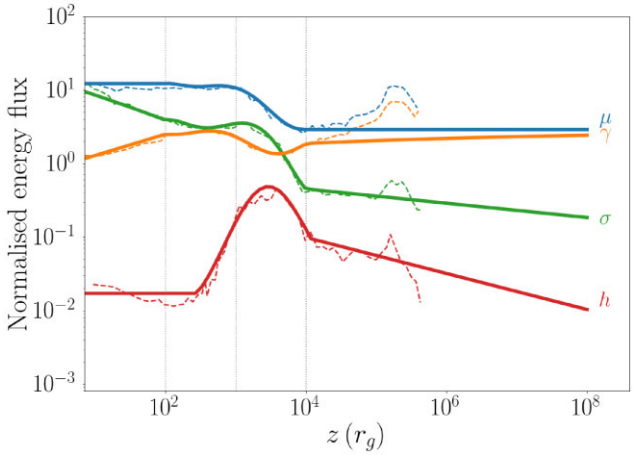

Figure 5. The energy flux components of a mass loaded jet, where μ is the ratio between the total energy flux and the rest-mass flux, γ is the bulk Lorentz factor, σ is the magnetisation, and h is the specific enthalpy. The mass entrainment occurs between 10^2 and $10^4\, r_g$ (vertical lines), but the entrained matter becomes comparable to the mass of the jet at a distance of $10^3\, \mathrm{r_g}$ (middle vertical line). Finally, we overplot with dashed lines the fiducial model B10 of CLTM19 on which we base our analysis (see Section 4).

4.1 Mass loading region

In this section, we present the parametrization of the values of σ, γ, and h of the mass loading region based on the B10 model described above. In particular, we fit a polynomial to the CLTM19 profiles along the jet between $z_{\rm diss} = 100\, r_g$ and $z_{\rm load,\,end} = 10^4\, r_g$. The profiles of the three quantities σ, γ, and h are hard to predict in such a complex and non-linear system, we hence decide to fit only for these three quantities and derive μ from equation (18).

Table 2. The fixed and the free (fitted) parameters that drive the mass loading jet dynamics. See Section 4 for further information.

Parameter	Fiducial value(s)	Definition	Status
γ_0	1.11	bulk Lorentz factor at the jet base z_0	fixed
σ_0	$10-50$	magnetisation of the flow at the jet base	free
$k_B T_e$ /keV	500	electron peak energy at the jet base	free
$\gamma_{\rm acc}$	$2-10$	bulk Lorentz factor at $z_{\rm acc}$	free
$h_{\rm acc}$	h_0[†]	jet specific enthalpy at $z_{\rm acc}$	fixed
f_ρ	10	jet mass density increase factor	fixed
$z_{\rm diss}/r_g$	100	region where the mass entrainment initiates[‡]	free
$z_{\rm load,\,end}/z_{\rm diss}$	100	region where the mass entrainment finishes	fixed

Notes.[†]calculated by the temperature of the electrons at the jet base (see equation 10), [‡]same as $z_{\rm acc}$.

$$\log_{10}(\sigma) = 0.621\,x^5 - 3.005\,x^4 + 4.599\,x^3 - 2.502\,x^2 + 0.242\,x + 0.563, \quad (28)$$

$$\log_{10}(\gamma) = -0.276\,x^6 + 1.412\,x^5 - 2.207\,x^4 + 0.853\,x^3 + 0.257\,x^2 - 0.075\,x + 0.394, \quad (29)$$

$$\log_{10}(h) = 0.467\,x^5 - 1.903\,x^4 + 1.100\,x^3 + 2.482\,x^2 - 1.171\,x - 1.826, \quad (30)$$

where $x = \log_{10}(z/z_{\rm diss})$ and $1 \leq x \leq \log_{10}\left(z_{\rm diss}/z_{\rm load,\,end}\right)$.

We connect the jet base to the mass loading region assuming that the specific enthalpy is constant to its initial value at the jet base as we calculate it with equation (10). We assume that the flow is launched at some speed equal to the speed of sound (see equation 1) and reaches a value $\gamma_{\rm acc}$, which is a free parameter, following a logarithmic dependence. In Table 2, we show the parameters of the mass loading jet model, indicating whether they are fixed or fitted parameters.

4.2 Jet segments beyond the mass loading region

Given our assumption that once mass-loading stops, the total energy flux is again conserved, i.e. μ is constant. Thus, we fix μ at its value at the end of the mass loading region, and to better constrain the profile of σ and h beyond the mass-loading region, we fit a first order polynomial between 10^4 and 10^5 r_g, with coefficients:

$$\log_{10}(\sigma) = -0.097\,x - 0.178, \quad (31)$$

$$\log_{10}(h) = -0.245\,x - 0.576, \quad (32)$$

where x is the same as above. Here, we choose to interpolate the profile of σ and h from the simulation data that closely follows the expected slow acceleration profile seen in semi-analytical MHD solutions of particle-dominated ($\sigma \lesssim 1$) jets (see e.g. Tchekhovskoy et al. 2009).

Having derived the values of μ, σ, and h, we calculate the bulk Lorentz factor for every jet segment above the $z_{\rm diss}$

$$\gamma(z \geq z_{\rm diss}) = \frac{\mu}{\sigma + h + 1}. \quad (33)$$

4.3 Particle acceleration and mass loaded jets

At the location where matter is entrained into the jets, particles start to accelerate to non-thermal energy as well. Based on the definition of h, we solve for the energy density of the protons

$$U_p = \frac{h\rho c^2 - \Gamma_e U_e}{\Gamma_p}, \quad (34)$$

where we calculate U_e from equation (11) for an MJ + non-thermal power-law distribution of electrons with a fixed ratio of 10 per cent between the thermal and the non-thermal electrons, and a fixed power-law slope p. We finally, derive the normalization of the non-thermal protons

$$K_p = \frac{U_p}{{\rm m_p c^2} \int \varepsilon^{-{\rm p}+1} \exp(-\varepsilon/\varepsilon_{\rm max}) {\rm d}\varepsilon}. \quad (35)$$

Following the above approach, we manage to self-consistently connect the mass loading that leads to an increase of the specific enthalpy h to the electromagnetic radiation due to the proton acceleration.

5 RESULTS FOR MASS LOADED JETS

5.1 Total energy flux evolution for mass loaded jets

In Fig. 6, we present the energy components for two different mass-loaded jets following the prescription of Section 4. We assume that both jets are Poynting flux dominated at the jet base with an initial magnetisation of $\sigma_0 = 40$ and accelerate to a bulk Lorentz factor of $\gamma_{\rm acc} = 3$. In the left-hand panel, we assume one electron per proton at the jet base $\eta_e = 1$, and in the right, we assume a pair-dominated jet of $\eta_e = 10000$. In both cases, we set the temperature of the thermal electrons at the jet base at $k_B T_e = 200\,{\rm keV}$. In the particular case of the pair-dominated jets, the specific enthalpy reaches values that are comparable to or even exceeding that of the bulk Lorentz factor and the magnetisation, especially at the loading region (see also equation 27). Despite the initially pair-dominated jet base, the matter entrained into the jets is in approximately equal number of electrons and protons because we assume that the most likely composition of an accretion disc wind is a neutral gas of electrons and protons. The jet composition hence changes from pair-dominated at the regions before the loading to almost equal number of protons and pairs (Anglés-Castillo et al. 2020).

In the right-hand panel of Fig. 6, we see that the increased number of pairs at the jet base leads to an increase of h. In the extreme case where $\eta_e \gg 1000$, the peak of the profile of h may lead to an artificial and unphysical increase of μ in the loading region. In Appendix C, we discuss how we constrain the increase of h to avoid such an artificial 'mass-loss'.

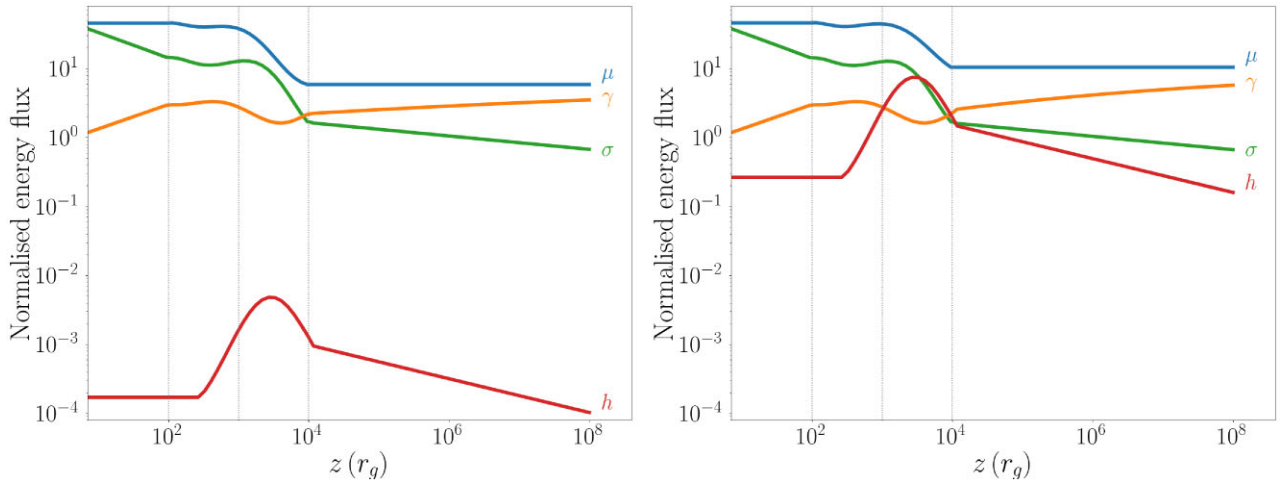

Figure 6. Similar to Fig. 5, but for: *left* an initial lepton temperature at the jet base of $k_B T_e = 200\,\mathrm{keV}$ and one electron per proton ($\eta_e = 1$), and in the *right* for a pair-dominated jet ($\eta_e = 10000$). Both scenarios are for an initial magnetisation of $\sigma_0 = 40$ and $\gamma_{\rm acc} = 3$.

5.2 Electromagnetic spectra of steady state mass-loaded jets

In Fig. 7, we plot in the left the predicted SED of the fiducial mass-loaded jet model based on the dynamical quantities that we show in Fig. 5. We further assume a jet base of radius $10\,r_g$, an electron temperature of 200 keV at the jet base, an injected jet power of $10^{-3}\,L_{\rm Edd}$ and the power-law slope of the accelerated particles $p = 2.2$ for both leptons and protons. Similar to above, we show the contribution of the leptonic emission of the jet segments before the dissipation/loading region, the leptonic contribution from the dissipation/loading region and beyond, and the hadronic contribution that is due to pγ. In the right subplot, we show the spectrum of a non-loaded jet with similar initial conditions. The main differences are in the jet emission from the jet base (yellow-shaded region) and the hadronic contribution. The jet-base emission is higher in the non-loaded case due to the magnetisation profile we assume here that leads to greater values for the first few jet segments up to the acceleration region (see e.g. Fig. 2).

In Fig. 8, we plot the SEDs that correspond to the two models of Fig. 6, where we account for mass loading at a distance $100\,r_g$, and we assume the injected jet power to be $10^{-3}\,L_{\rm Edd}$. We show the different components of the spectrum in Appendix D.

6 DISCUSSION

6.1 Steady state jets

In the first part of this work, we present the analytical jet model that includes the specific enthalpy in the jet kinematics and the spatial evolution.

6.1.1 *Specific enthalpy, particle acceleration, and jet evolution*

The specific enthalpy h is a good estimate of whether a jet is cold or hot, with values of $h \ll 1 + \sigma$ to indicate a cold flow, and values of $h \gtrsim 1 + \sigma$ to indicate a hot flow. Astrophysical jets launched by black holes are overall considered cold and strongly magnetised. The majority of semi-analytical models that focus on the radiative output rather than the detailed description of the jets, neglect the specific enthalpy for simplicity (Markoff et al. 2005; Bosch-Ramon, Romero & Paredes 2006; Vila, Romero, G. E. & Casco, N. A. 2012; Zdziarski et al. 2014). When particles accelerate though, and in particular in the case where these accelerated particles carry a significant fraction of the jet energy, the specific enthalpy increases. As we show in Fig. 1, the exact value of the specific enthalpy may get values that can easily compare to the bulk Lorentz factor (values of the order of 1 and ∼10) and/or the jet magnetisation (values greater than unity for a magnetised outflow). The exact value of h strongly depends on three aspects: the matter composition of the jet, the efficiency of the leptonic acceleration, and whether hadrons accelerate as well or not.

Leptonic acceleration: In the case where only leptons accelerate inside the jets, we expect the electron average Lorentz factor to increase as the acceleration efficiency increases (top subplots of Fig. 1) and hence the specific enthalpy to increase as well, according to equation (27). The total specific enthalpy however depends on the jet composition as well. When a jet is of one electron per proton ($\eta_e = 1$), the values of h are ∼0.01 regardless of the exact average Lorentz factor of the electrons (as long as the average Lorentz factor of the leptons remains less than $\mathrm{m_p/m_e} \simeq 1836$). This is the typical scenario that current GRMHD and semi-analytical jet models consider when studying the exact jet evolution, both in space and time. As we mention above though, based on observations of both extragalactic and Galactic jets, it is very likely that jets are pair-dominated (or at least the scenario of one proton per electron is disfavoured in some cases). Such a jet content leads to an increase in the specific enthalpy compared to the case of $\eta_e = 1$ (see equation 27). The specific enthalpy hence of a jet that is pair-dominated at launching may contribute significantly to the spatial evolution of the jet, and the more relativistic (or warmer) the distribution of pairs, the larger the impact of h on the jet evolution. A pair dominated jet, in fact, requires specific enthalpy that can be two to three orders of magnitude larger than the jet case of an equal number of electrons and protons (see e.g. top plots of Fig. 1). Consequently, to achieve bulk flow acceleration up to the same bulk Lorentz factor, a pair-dominated jet, also requires a larger value of magnetisation at the jet base if energy flux is conserved along the jet.

Lepto-hadronic acceleration: The energy content of the particles can further increase when jets accelerate both leptons and hadrons

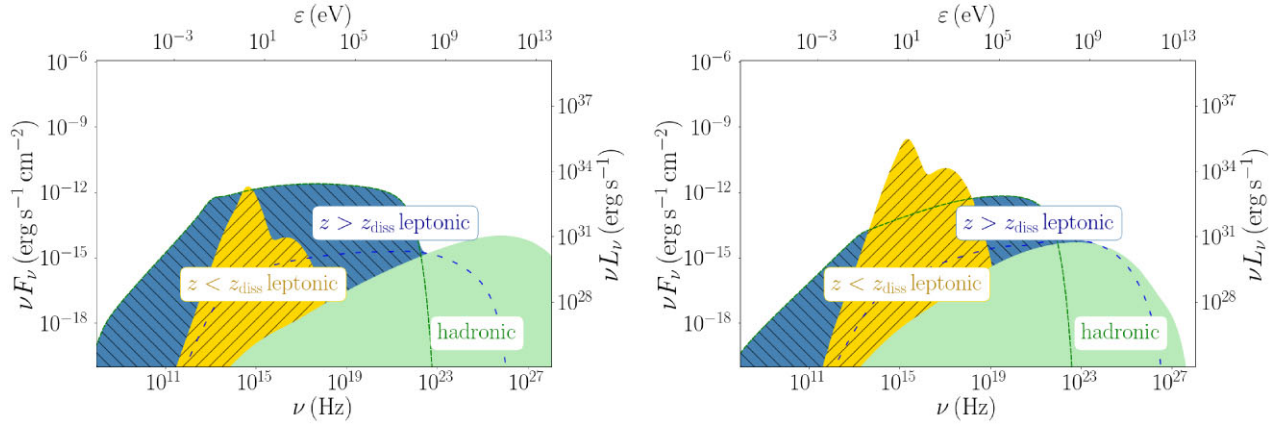

Figure 7. *Left*: The predicted spectral energy distribution of a mass-loaded jet that corresponds to the dynamical quantities of Fig. 5 for a 10 $M_\odot$ BHXB at 3 kpc. We assume a jet base of 200 keV and radius of 10 r_g. We show the contribution of the jet-segments before the mass loading (yellow-shaded region), and the contribution of the mass-loaded segments of both leptonic (blue-shaded) and hadronic (green-shaded). The hadronic contributes includes both the neutral pion decay and the synchrotron radiation of the secondary electrons/positrons. *Right*: Similar to the left, but for a non-loaded jet with similar initial conditions.

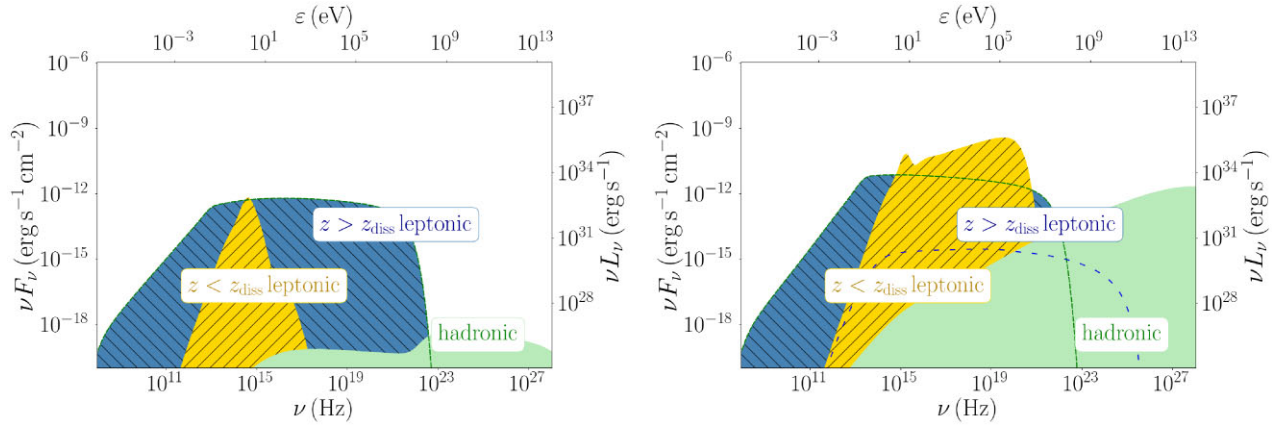

Figure 8. Similar to Fig. 7 but for the mass-loaded jets that correspond to the dynamical quantities of Fig. 6.

to non-thermal energies. In fact, the more efficient the particle acceleration, the larger the specific enthalpy, which may get values of the order of $\Gamma_p\langle\varepsilon_p\rangle$, regardless of the jet content, as long as $\eta_e \leq {\rm m_p/m_e}$ (Fig. 1). It is hard to predict the exact value of the specific enthalpy in a jet that efficiently accelerates particles, but overall, it may get values equal to or even exceed that of the bulk Lorentz factor and/or the magnetisation, that would mean that the outflow converts to particle dominated instead. We hence suggest that the specific enthalpy should be treated with extra care and should not always be considered negligible.

6.1.2 *Specific enthalpy and spectrum*

The SED of the steady jets strongly depends not only on the hadronic acceleration (or lack of it), but also on the jet content. The most important difference is in the GeV-to-TeV spectrum. A pair dominated jet is characterized by the ICS and any contribution from the hadronic processes is suppressed. In the case of a jet with equal number of protons and pairs, and accounting for an efficient hadronic acceleration, the hadronic component dominates in the GeV/TeV bands via the neutral pion decay, which has a distinguishable shape than that of ICS in the Klein–Nishina regime.

The IR-to-X-ray spectrum of BHXBs may be contaminated by different components, such as the companion star and/or the accretion disc. In the case of a pair-dominated jet, though, the X-ray spectrum shows the multiple Compton scatterings due to the increased electron density that can potentially replicate the role of the theoretical corona (Markoff et al. 2005, 2015; Cao et al. 2021; Lucchini et al. 2021). Such an X-ray signature can prove a useful tool to distinguish between different jet compositions, especially with the next-generation X-ray telescopes, such as for instance the Imaging X-ray Polarimetry Explorer (IXPE; Weisskopf et al. 2016), the Advanced Telescope for High-energy Astrophysics (Athena; Nandra et al. 2013), and the Advanced X-ray Imaging Satellite (AXIS; Mushotzky et al. 2019).

6.2 Mass-loaded jets – `HadJet`

The initial jet composition at the jet base significantly alters the specific enthalpy of the jet along its axis, even if we assume that at the mass loading region the jet converts to a pair-proton outflow. We see, in particular, that a pair-proton jet base with a thermal pair distribution that peaks at some energy of the order of 500 keV, which is a reasonable value for BHXBs, resulting in insignificant specific enthalpy compared to the rest energy components, namely

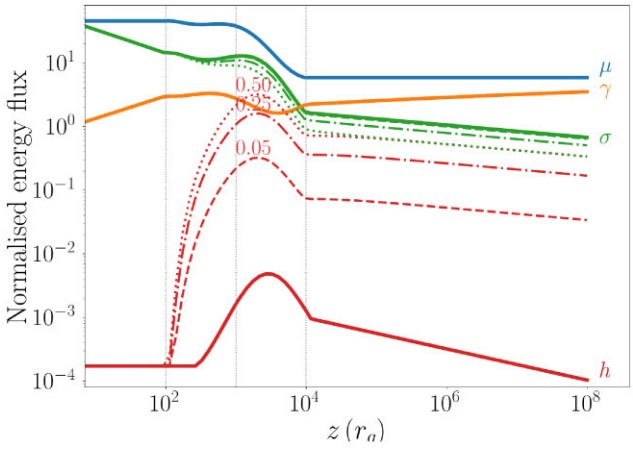

Figure 9. Similar to the left sub-plot of Fig. 6, but with different $f_{\rm heat}$ parameters as shown in the plot.

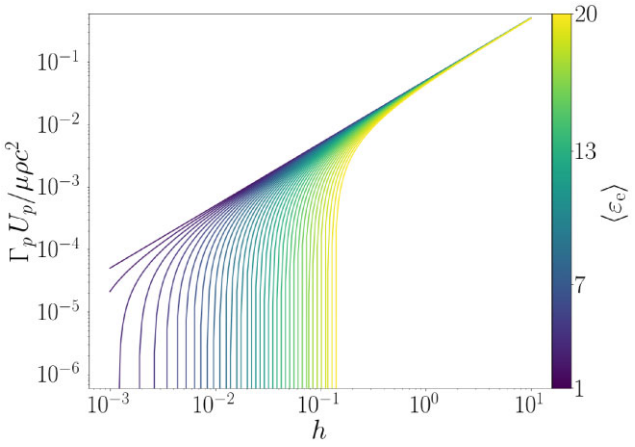

Figure 10. The specific enthalpy of the protons $\Gamma_p U_p/\rho c^2$ divided by μ shows the total energy that is allocated to protons with respect to the total available jet energy, as a function of the jet specific enthalpy h. We plot the proton energy density for a number of different electron energy densities that correspond to different values of $\langle\varepsilon_e\rangle$ as shown in the colour map, and we use $\eta_e = 10$.

the magnetisation and the bulk Lorentz factor (see e.g. the left subplot of Fig. 6). If the jet base, on the other hand, is pair-dominated, then similar to our discussion above, the initial specific enthalpy at the jet base is increased, and hence its effect on the jet dynamical evolution might be more important because the energy content carried by particles might be similar to the bulk kinetic energy (see e.g, the right subplot of Fig. 6).

The initial conditions at the jet base have a significant impact on the electromagnetic spectrum that is our tool to distinguish between the different scenarios. For the two different scenarios we study here, where the one shows a pair-proton jet base and the other a pair dominated jet base, there are two prominent differences in the multiwavelength SEDs. The most important one is in the GeV/TeV regime, where the larger specific enthalpy of the initially pair-dominated jet base allows for more energy to be transferred to protons. The increased energy available for non-thermal proton acceleration allows for a stronger TeV flux, which is dominated by the neutral pion decay due to pγ interactions. Such TeV flux, depending on the distance of the BHXB (see e.g. Kantzas et al. 2022) might be significant to be detected by current TeV facilities, such as the Large High Altitude Air Shower Observatory (LHAASO) or future γ-ray facilities, such as the Cherenkov Telescope Array (CTA). The fact that an initially pair dominated jet can potentially lead to a stronger TeV flux may sound counterintuitive, but in fact it is natural in our treatment due to the assumption that the mass loading is linked with energy dissipation into particle acceleration. The increase of the specific enthalpy depends on the initial conditions of the jet launching, and in this work, we base our formalism on one specific set up of GRMHD simulations. A different set up is very likely to lead to less efficient heating of the jets, the specific enthalpy nevertheless will still increase due to energy transfer (see discussion of CLTM19). To explore the full range of possible physical scenarios with GRMHD simulations is currently too computationally expensive. We can however examine semi-analytically how the impact on the jet kinematics depends on the level of dissipation by replacing the heating parameter $f_{\rm heat}$ (that was used in previous work to estimate the heating of the thermal particles at the particle acceleration region; see e.g. discussion in Lucchini et al. 2021) with the fraction of the magnetic energy that is additionally allowed to go into energising particles. With such a parametrization, h will increase by a factor $f_{\rm heat}\sigma$ along the jet, whereas the magnetisation will be reduced as $(1 - f_{\rm heat})\sigma$. We show in Fig. 9 the impact of this free parameter in the energy components. To avoid a steep increase of h that looks like a step-function, we use a function $\tanh^2(z/z_{\rm diss})$ instead. The underlying model is that of the left-hand panel of Fig. 6, where we assume a 'hot' jet base (500 keV) and one proton per electron.

A further spectral difference between a pair-proton and a pair-dominated jet base is in the lower energy regime of the spectrum, and in particular, in the UV-to-X-ray spectrum. For the same initial magnetisation and injected power, the number density of the pairs at the pair-dominated jet base is enhanced (see e.g. equation 16) resulting in increased Compton scatterings that lead to a significant difference in the ∼1–100 keV range. The X-ray spectrum in particular shows a hard spectral index ($\nu F_\nu \propto \nu^{-\alpha+1}$, with $\alpha < 1$; see right-hand plot in Fig. 8) that is similar to the expected output of a thermal corona (Sunyaev & Titarchuk 1980; Haardt & Maraschi 1993; Narayan & Yi 1994; Titarchuk 1994; Magdziarz & Zdziarski 1995).

6.3 Proton energy crisis

With the conserved mass loading jet model we develop here, we are able to constrain the total energy that is allocated to the protons and is used to accelerate them to non-thermal energies. In that way, the total energy carried by the accelerated protons never exceeds the available energy of the jets that has been a major issue in the past (Böttcher et al. 2013; Zdziarski & Böttcher 2015; Liodakis & Petropoulou 2020; Kantzas et al. 2022). In Fig. 10, we plot the specific enthalpy of the protons $\Gamma_p U_p/\rho c^2$ divided by μ as a function of the total jet enthalpy h. This quantity expresses the fraction of the total energy flux of the jet that is used by the accelerated protons, and we show its dependence on h for different average electron Lorentz factors, as indicated by the colour map. Regardless of the average electron energy $\langle\varepsilon_e\rangle$, the protons can hardly carry more than ∼10 per cent of the total energy in the jets because higher fractions would require specific enthalpy h of the order of a few or above (upper-right corner of the plot) resulting in strongly magnetised flows ($\sigma \gtrsim \gamma h$). Moreover, the protons can only be accelerated if the total specific enthalpy h is greater than some critical value $h > h_{\rm crit}$ where

$$h_{\rm crit} = \frac{(\langle\varepsilon_e\rangle - 1)\Gamma_e}{1 + \frac{\rm m_p/m_e}{\eta_e}}, \tag{36}$$

hence the cut offs for different $\langle \varepsilon_e \rangle$ at small values of h. In this particular figure, we use $\eta_e = 10$, but as we show in Appendix E for smaller (larger) values of η_e the only difference is that the cut offs are located to smaller (larger) values of h.

From Fig. 10, we see that the energy of the accelerated protons never exceeds that of the jet because the specific enthalpy of the non-thermal protons is always less than the total normalized energy flux ($\Gamma_p U_p / \rho c^2 < \mu$) and hence never violates the energy budget.

7 SUMMARY AND CONCLUSIONS

Relativistic jets are efficient CR accelerators, but we still do not fully understand the particle acceleration mechanism. To fully interpret the jet kinematics, and how they relate to particle acceleration, we need to better understand how to link the observed spectra emitted by jetted sources over more than ten orders of magnitude in photon frequency to the jet physical properties. Currently uncertainties about the composition as well as a lack of conserved dynamical models have contributed to a degeneracy between leptonic and lepto-hadronic models.

To break this degeneracy, we have developed a new multi-zone approach that links the jet composition to the jet dynamics. The total energy flux along the jet is conserved, while magnetic energy can be dissipated into both kinetic energy and gas enthalpy via particle acceleration. This new approach makes clear the key role that the specific enthalpy h can have on the evolution and exchange of energy along the jet. In particular the enthalpy should be explicitly taken into account in models where: i) Electrons accelerate to large average energies, ii) protons accelerate in the jets as well, and/or iii) when the jet is pair-dominated, as suggested for numerous Galactic and extragalactic jets launched by black holes.

When protons are accelerated into a non-thermal power law, the energy requirement often exceeds the total energy that can be provided by the jet and/or the accretion energy on to the black hole, potentially violating energy conservation. We have developed a new model `HadJet` based on our earlier lepto-hadronic work, that now conserves energy and includes a prescription for proton entrainment. Such a mass loading may in fact inhibit proton acceleration. By allowing the jets to entrain protons over a range of distance, as seen to occur in GRMHD simulations via eddies forming at the jet/accretion disc interface (CLTM19), we demonstrate a new method to avoid the 'hadronic power' problem in a more self-consistent approach. In a future work, we plan to further explore the impact of mass loading on the multiwavelength emission of both BHXB jets and AGN jets.

ACKNOWLEDGEMENTS

We would like to thank the anonymous reviewer for the thorough commenting that significantly improved the manuscript. DK and SM are grateful for support by the Netherlands Organisation for Scientific Research (NWO) VICI grant (number 639.043.513). KC is supported by the Black Hole Initiative at Harvard University, which is funded by grants from the Gordon and Betty Moore Foundation, John Templeton Foundation, and the Black Hole PIRE program (NSF grant OISE-1743747).

DATA AVAILABILITY

No new data were generated or analysed in support of this research.

REFERENCES

Aartsen M. et al., 2018, Science, 361, 1378
Abbasi R. U. et al., 2019, Phys. Rev. D, 99, 022002
Abbasi R. U. et al., 2020, ApJ, 898, L28
Aharonian F. A., 2004, Very High Energy Cosmic Gamma Radiation: A Crucial Window on the Extreme Universe. World Scientific Press, Singapore
Aloisio R., Berezinsky V., Gazizov A., 2012, Astropart. Phys., 39, 129
Anglés-Castillo A., Perucho M., Martí J. M., Laing R. A., 2020, MNRAS, 500, 1512
Ball D., Sironi L., Özel F., 2018, ApJ, 862, 80
Begelman M. C., 1998, ApJ, 493, 291
Begelman M. C., Blandford R. D., Rees M. J., 1984, Rev. Mod. Phys., 56, 255
Beskin V. S., 2010, Phys. Usp., 53, 1199
Beskin V. S., Nokhrina E. E., 2006, MNRAS, 367, 375
Blandford R., Königl A., 1979, ApJ, 232, 34
Blandford R. D., Payne D. G., 1982, MNRAS, 199, 883
Blandford R. D., Rees M. J., 1974, MNRAS, 169, 395
Blandford R. D., Znajek R. L., 1977, MNRAS, 179, 433
Blumenthal G. R., Gould R. J., 1970, Rev. Mod. Phys., 42, 237
Bodo G., Mamatsashvili G., Rossi P., Mignone A., 2021, MNRAS, 510, 2391
Bogovalov S., Tsinganos K., 2005, MNRAS, 357, 918
Bosch-Ramon V., Romero G. E., Paredes J. M., 2006, A&A, 447, 263
Böttcher M., Baring M. G., 2019, ApJ, 887, 133
Böttcher M., Reimer A., Sweeney K., Prakash A., 2013, ApJ, 768, 54
Bowman M., Leahy J. p., Komissarov S. S., 1996, MNRAS, 279, 899
Broderick A. E., Tchekhovskoy A., 2015, ApJ, 809, 97
Bromberg O., Tchekhovskoy A., 2015, MNRAS, 456, 1739
Cao Z., Lucchini M., Markoff S., Connors R. M. T., Grinberg V., 2021, MNRAS, 509,
Celotti A., Fabian A. C., 1993, MNRAS, 264, 228
Chatterjee K., Liska M., Tchekhovskoy A., Markoff S. B., 2019, MNRAS, 490, 2200 (CLTM19)
Connors R. M. T. et al., 2019, MNRAS, 485, 3696
Cooper A. J., Gaggero D., Markoff S., Zhang S., 2020, MNRAS, 493, 3212
Coppi P., Blandford R., 1990, MNRAS, 245, 453
Corstanje A. et al., 2021, Phys. Rev. D, 103, 102006
Crumley P., Ceccobello C., Connors R. M. T., Cavecchi Y., 2017, A&A, 601, A87
Díaz Trigo M., Miller-Jones J. C., Migliari S., Broderick J. W., Tzioumis T., 2013, Nature, 504, 260
Drenkhahn G., Spruit H. C., 2002, A&A, 391, 1141
Eichler D., 1993, ApJ, 419, 111
Fabrika S., 2004, Astrophys. Space Phys. Reviews, 12, 1
Falcke H., Biermann P. L., 1995, A&A, 293, 665
Falcke H., Körding E., Markoff S., 2004, A&A, 414, 895
Fender R. P., Maccarone T. J., van Kesteren Z., 2005, MNRAS, 360, 1085
Gallo E., Fender R., Kaiser C., Russell D., Morganti R., Oosterloo T., Heinz S., 2005, Nature, 436, 819
Ghisellini G., Tavecchio F., 2010, MNRASL, 409, L79
Ghisellini G., Tavecchio F., Maraschi L., Celotti A., Sbarrato T., 2014, Nature, 515, 376
Giannios D., Spruit H. C., 2006, A&A, 450, 887
Giannios D., Kylafis N. D., Psaltis D., 2004, A&A, 425, 163
Gourgouliatos K. N., Komissarov S. S., 2018, Nature Astron., 2, 167
Granot J., Komissarov S. S., Spitkovsky A., 2011, MNRAS, 411, 1323
Guo F., Li H., Daughton W., Liu Y.-H., 2014, Phys. Rev. Lett., 113, 155005
Haardt F., Maraschi L., 1993, ApJ, 413, 507
Hailey C. J., Mori K., Bauer F. E., Berkowitz M. E., Hong J., Hord B. J., 2018, Nature, 556, 70
Heinz S., 2006, ApJ, 636, 316
Heinz S., Sunyaev R. A., 2003, MNRAS, 343, L59
Hillas A. M., 1984, ARA&A, 22, 425
Hjellming R., Johnston K., 1988, ApJ, 328, 600
Jokipii J., 1987, ApJ, 313, 842
Kantzas D. et al., 2021, MNRAS, 500, 2112
Kantzas D., Markoff S., Lucchini M., Ceccobello C., Grinberg V., Connors R. M. T., Uttley P., 2022, MNRAS, 510, 5187
Kelner S., Aharonian F., 2008, Phys. Rev. D, 78, 034013
Kelner S., Aharonian F. A., Bugayov V., 2006, Phys. Rev. D, 74, 034018

Komissarov S. S., Barkov M. V., Vlahakis N., Königl A., 2007, MNRAS, 380, 51
Komissarov S. S., Vlahakis N., Königl A., Barkov M. V., 2009, MNRAS, 394, 1182
Königl A., 1980, Phys. Fluids, 23, 1083
Liodakis I., Petropoulou M., 2020, ApJ, 893, L20
Liodakis I., Blinov D., Potter S. B., Rieger F. M., 2021, MNRASL, 509, L21
Lister M. L., Homan D. C., Kadler M., Kellermann K. I., Kovalev Y. Y., Ros E., Savolainen T., Zensus J. A., 2009, ApJ, 696, L22
Lister M. L. et al., 2016, AJ, 152, 12
Lucchini M., Markoff S., Crumley P., Krauß F., Connors R. M. T., 2018, MNRAS, 482, 4798
Lucchini M., Russell T. D., Markoff S. B., Vincentelli F., Gardenier D., Ceccobello C., Uttley P., 2021, MNRAS, 501, 5910
Lucchini M. et al., 2022, MNRAS, 517, 5853
McKinney J. C., 2006, MNRAS, 368, 1561
Magdziarz P., Zdziarski A. A., 1995, MNRAS, 273, 837
Maitra D., Markoff S., Brocksopp C., Noble M., Nowak M., Wilms J., 2009, MNRAS, 398, 1638
Mannheim K., 1993, A&A, 269, 67
Mannheim K., Schlickeiser R., 1994, A&A, 286, 983
Markoff S., Falcke H., Fender R., 2001, A&A, 372, L25
Markoff S., Nowak M., Corbel S., Fender R., Falcke H., 2003, A&A, 397, 645
Markoff S., Nowak M. A., Wilms J., 2005, ApJ, 635, 1203
Markoff S. et al., 2015, ApJ, 812, L25
Matthews J. H., Bell A. R., Blundell K. M., 2020, New Astron. Rev., 89, 101543
Merloni A., Heinz S., Di Matteo T., 2003, MNRAS, 345, 1057
Mignone A., Striani E., Tavani M., Ferrari A., 2013, MNRAS, 436, 1102
Mirabel I., Rodriguez L., 1994, Nature, 371, 46
Moll R., Spruit H. C., Obergaulinger M., 2008, A&A, 492, 621
Mori K. et al., 2021, ApJ, 921, 148
Mushotzky R. et al., 2019, BAAS, 51, 107
Nandra K. et al., 2013, preprint (arXiv:1306.2307)
Narayan R., Yi I., 1994, AJ, 428, L13
Nokhrina E. E., Beskin V. S., Kovalev Y. Y., Zheltoukhov A. A., 2015, MNRAS, 447, 2726
Olejak A., Belczynski K., Bulik T., Sobolewska M., 2020, A&A, 638, A94
Parfrey K., Philippov A., Cerutti B., 2019, Phys. Rev. Lett., 122, 035101
Pepe C., Vila G. S., Romero G. E., 2015, A&A, 584, A95
Petropoulou M., Sironi L., Spitkovsky A., Giannios D., 2019, ApJ, 880, 37
Petropoulou M., Psarras F., Giannios D., 2022, MNRAS, 518, 2719
Polko P., Meier D. L., Markoff S., 2014, MNRAS, 438, 959
Porth O., Komissarov S. S., 2015, MNRAS, 452, 1089
Potter W. J., Cotter G., 2012, MNRAS, 429, 1189
Protheroe R. J., Kazanas D., 1983, ApJ, 265, 620
Pushkarev A. B., Kovalev Y. Y., Lister M. L., Savolainen T., 2009, A&A, 507, L33
Pushkarev A. B., Kovalev Y. Y., Lister M. L., Savolainen T., 2017, MNRAS, 468, 4992
Rachen J. P., Biermann P. L., 1993, A&A, 272, 161
Rachen J. P., Mészáros P., 1998, Phys. Rev. D, 58, 123005
Reig P., Kylafis N. D., Giannios D., 2003, A&A, 403, L15
Romero G. E., Torres D. F., Bernadó M. K., Mirabel I., 2003, A&A, 410, L1
Rybicki G. B., Lightman A. P., 2008, Radiative Processes in Astrophysics. Wiley, New York
Shikaze Y. et al., 2007, Astropart. Phys., 28, 154
Sironi L., Spitkovsky A., 2014, ApJ, 783, L21
Sironi L., Petropoulou M., Giannios D., 2015, MNRAS, 450, 183
Sironi L., Rowan M. E., Narayan R., 2021, ApJ, 907, L44
Spruit H. C., Foglizzo T., Stehle R., 1997, MNRAS, 288, 333
Sunyaev R. A., Titarchuk L. G., 1980, A&A, 86, 121
Tchekhovskoy A., McKinney J. C., Narayan R., 2008, MNRAS, 388, 551
Tchekhovskoy A., McKinney J. C., Narayan R., 2009, ApJ, 699, 1789
Tetarenko B. E., Sivakoff G. R., Heinke C. O., Gladstone J. C., 2016, ApJS, 222, 15
Tetarenko A. J. et al., 2021, MNRAS, 504, 3862
The Pierre Auger Observatory et al., 2017, Science, 357, 1266
Titarchuk L., 1994, ApJ, 434, 570
Vila G. S., Romero G. E., 2010, MNRAS, 403, 1457
Valia, Romero G. E., Casco N. A., 2012, A&A, 538, A97
Vlahakis N., Konigl A., 2003, ApJ, 596, 1080
Waggett P., Warner P., Baldwin J., 1977, MNRAS, 181, 465
Weisskopf M. C. et al., 2016, in den Herder J.-W. A., Takahashi T., Bautz M.eds, SPIE Conf. Ser. Vol. 9905, Space Telescopes and Instrumentation 2016: Ultraviolet to Gamma Ray. SPIE, Bellingham, p. 990517
Yushkov A., Collaboration P. A., others, 2019, ICRC, 358, 482
Zacharias M., Reimer A., Boisson C., Zech A., 2022, MNRAS, 512, 3948
Zanin R., Fernández-Barral A., de Oña Wilhelmi E., Aharonian F., Blanch O., Bosch-Ramon V., Galindo D., 2016, A&A, 596, A55
Zdziarski A. A., Böttcher M., 2015, MNRASL, 450, L21
Zdziarski A. A., Pjanka P., Sikora M., Stawarz Ł., 2014, MNRAS, 442, 3243
Zdziarski A. A., Tetarenko A. J., Sikora M., 2022a, ApJ, 925, 189
Zdziarski A. A., Phuravhathu D. G., Sikora M., Böttcher M., Chibueze J. O., 2022b, ApJ, 928, L9

APPENDIX A: SPECIFIC ENTHALPY FOR A HARD POWER LAW OF ACCELERATED PARTICLES

In Fig. A1 we plot the evolution of h for different jet composition. See Section 3.1 for a detailed description of the subplots. In this figure, we show the evolution of h assuming that the particles accelerate in a harder power law with an index of $p = 1.7$ compared to $p = 2.2$ we discuss in the main text.

In the top subplots, we notice a similar behaviour to Fig. 1 but h goes to larger values for the case of a pair-dominated jet ($h \sim \Gamma_e \langle \varepsilon_e \rangle$) according to equation 27).

In the case where protons accelerate as well, h can attain values as large as $\sim$2000 for a particle acceleration with $\varepsilon_{e,\,min} = \varepsilon_{p,\,min} = 10$ as we show in the lowermost subplots. This value is significantly larger than the expected values of γ of the bulk flow and in combination with the case where σ takes large values to lead to hard power laws of particles (Sironi et al. 2015,2021; Ball et al. 2018), we see that the equation $\mu = \gamma(\sigma + h + 1)$ (equation 18) would not be a good approximation for the bulk Lorentz factor anymore (McKinney 2006; Komissarov et al. 2007, 2009; Beskin 2010).

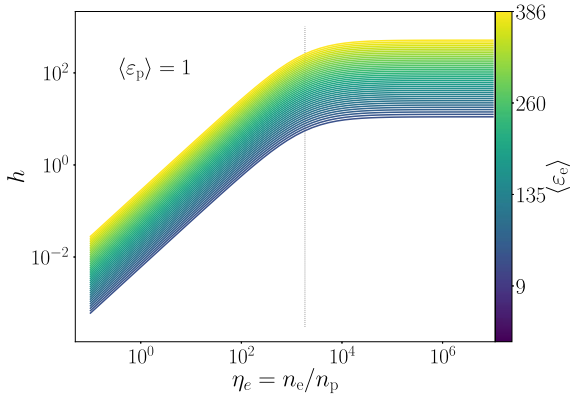

(a) Purely leptonic acceleration with $\varepsilon_{e,min} = 1.5$.

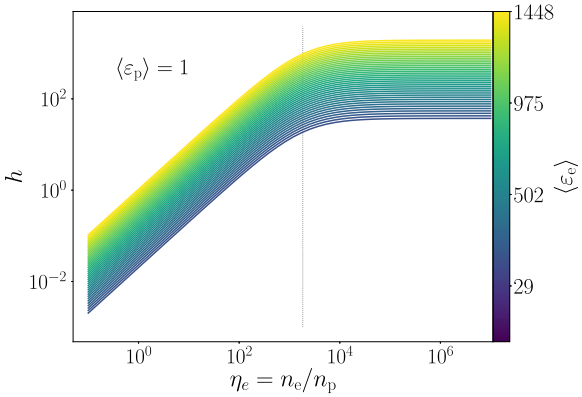

(b) Purely leptonic acceleration with $\varepsilon_{e,min} = 10$.

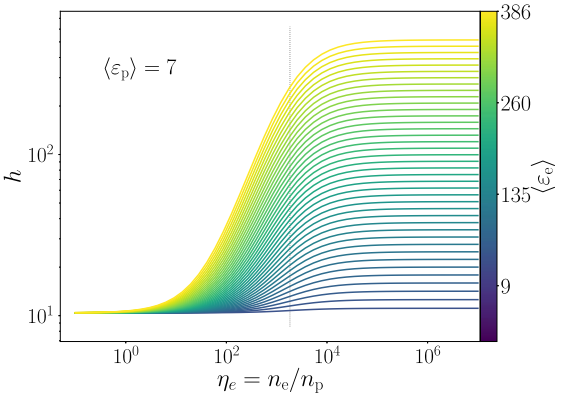

(c) Leptohadronic acceleration with $\varepsilon_{e,min} = 1.5$.

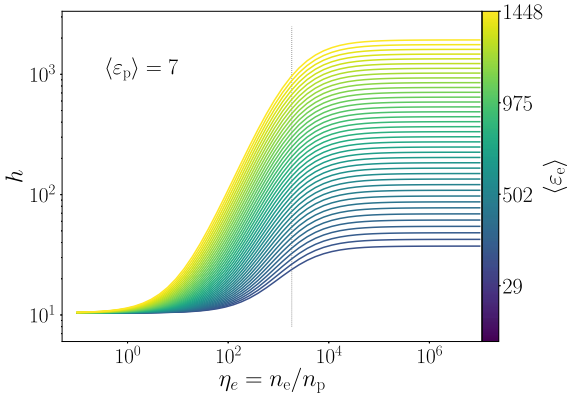

(d) Leptohadronic acceleration with $\varepsilon_{e,min} = 10$.

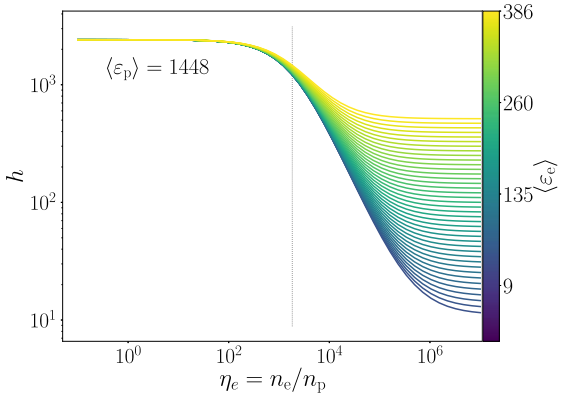

(e) More efficient hadronic, and leptonic acceleration with $\varepsilon_{e,min} = 1.5$.

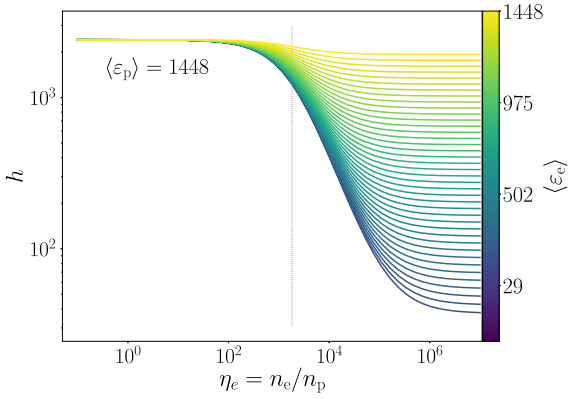

(f) More efficient hadronic, and leptonic acceleration with $\varepsilon_{e,min} = 10$.

Figure A1. The jet specific enthalpy h as a function of the jet content $\eta_e = n_e/n_p$. In all plots, we assume $p = 1.7$ to derive the average particle Lorentz factors from equation (25). The colour map corresponds to the average Lorentz factor of pairs with lighter colours to indicate larger values. In the left column, we set the minimum Lorentz factor of pairs to be $\varepsilon_{e,\,min} = 1.5$, and on the right column, we use $\varepsilon_{e,\,min} = 10$. In the top raw, we assume that only leptonic acceleration takes place, in the middle raw, we assume hadronic acceleration as well with $\varepsilon_{p,\,min} = 1$ and $\varepsilon_{p,\,max} = 100$, and in the bottom raw, we assume $\varepsilon_{p,\,min} = 10$ and $\varepsilon_{p,\,max} = 10^7$. The vertical lines correspond to $\eta_e = m_p/m_e$.

APPENDIX B: ALL ENERGY COMPONENTS PLOTS

In Figs B1-B4, we show the evolution of μ along the jet for different values of h. In particular, for all subplots of Figs B1–B4, we assume that the accelerated particles follow a power law with an index of $p = 2.2$. The outflow launches at a distance of $6\,r_g$ from the black hole and the particle acceleration initiates at $10^3\,r_g$. While the jets accelerate at some maximum Lorentz factor $\varepsilon_{acc} = 3$, we assume that the magnetisation at

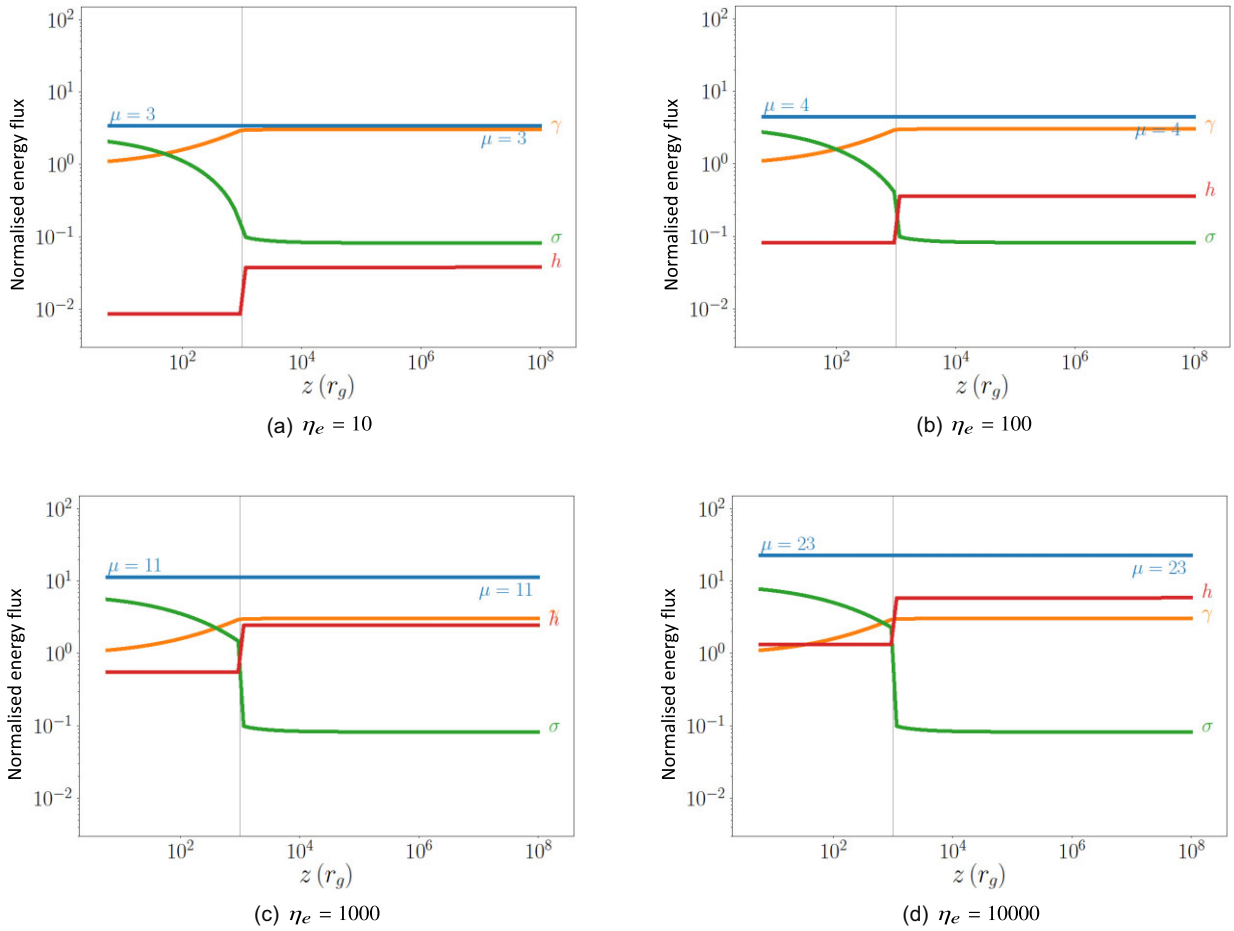

Figure B1. The evolution of the different energy components γ, σ, and h as indicated in each subplot, and the total μ based on equation (18). All subplots are for an average electron Lorentz factor of $\langle \varepsilon_e \rangle = 6$ and the jet content is shown in each subplot.

this region has dropped to $\sigma_{\rm acc} = 0.1$. For every subplot, we assume $\eta_e = 10$ (top left), $\eta_e = 100$ (top right), $\eta_e = 10^3$ (bottom left), and $\eta_e = 10^4$ (bottom right) constant along the outflow.

In Fig. B1, we plot the jet evolution assuming only leptonic acceleration with an average Lorentz factor of $\langle \varepsilon_e \rangle = 6$. In agreement with Fig. 1, we see that while the pair content increases in the jets, the specific enthalpy increases accordingly, and hence the total μ increases. In the cases of $\eta_e = 10^3$ and 10^4, in particular, we see that the specific enthalpy h has values comparable or even larger than the bulk Lorentz factor of the jet flow.

In Fig. B2, we plot a purely leptonic acceleration similar to Fig. B1 but assuming $\langle \varepsilon_e \rangle = 32$ instead. The pair-dominated jets where $\eta_e = 10^3$ and 10^4 (bottom subplots), indicate that an efficient acceleration mechanism would lead to high values of h, which for the case of $\eta_e = 10^4$ the overall value of μ is of the order of 100, a much higher value than commonly found in the literature.

In Figs B3 and B4, we further account for hadronic acceleration with $\langle \varepsilon_p \rangle = 4$. In the cases where the jets are pair-dominated, to obtain the specific enthalpy h calculated at the particle acceleration region, we require a jet base that is Poynting flux dominated with a magnetisation of the order of 50–100.

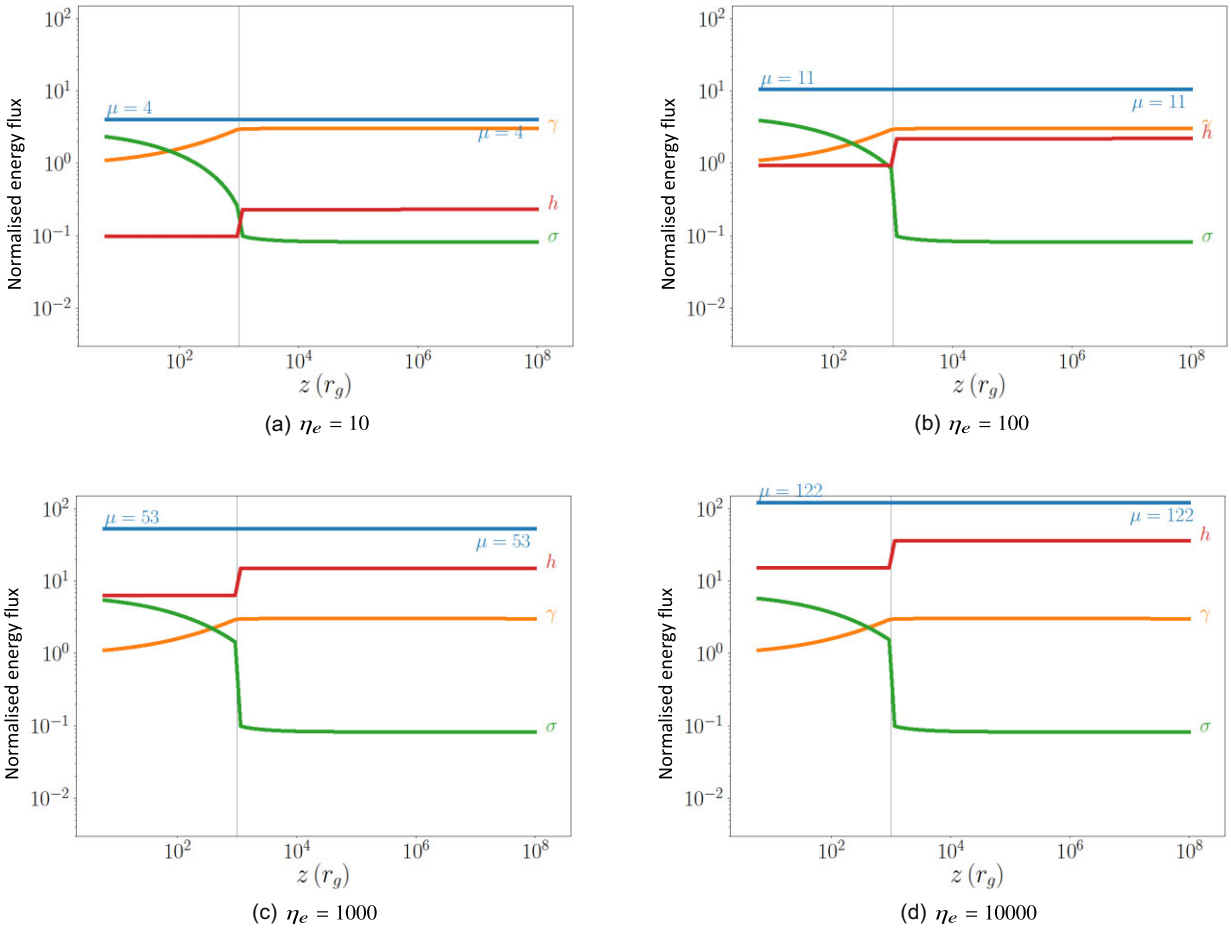

Figure B2. Same as Fig. B1 but for $\langle \varepsilon_e \rangle = 32$.

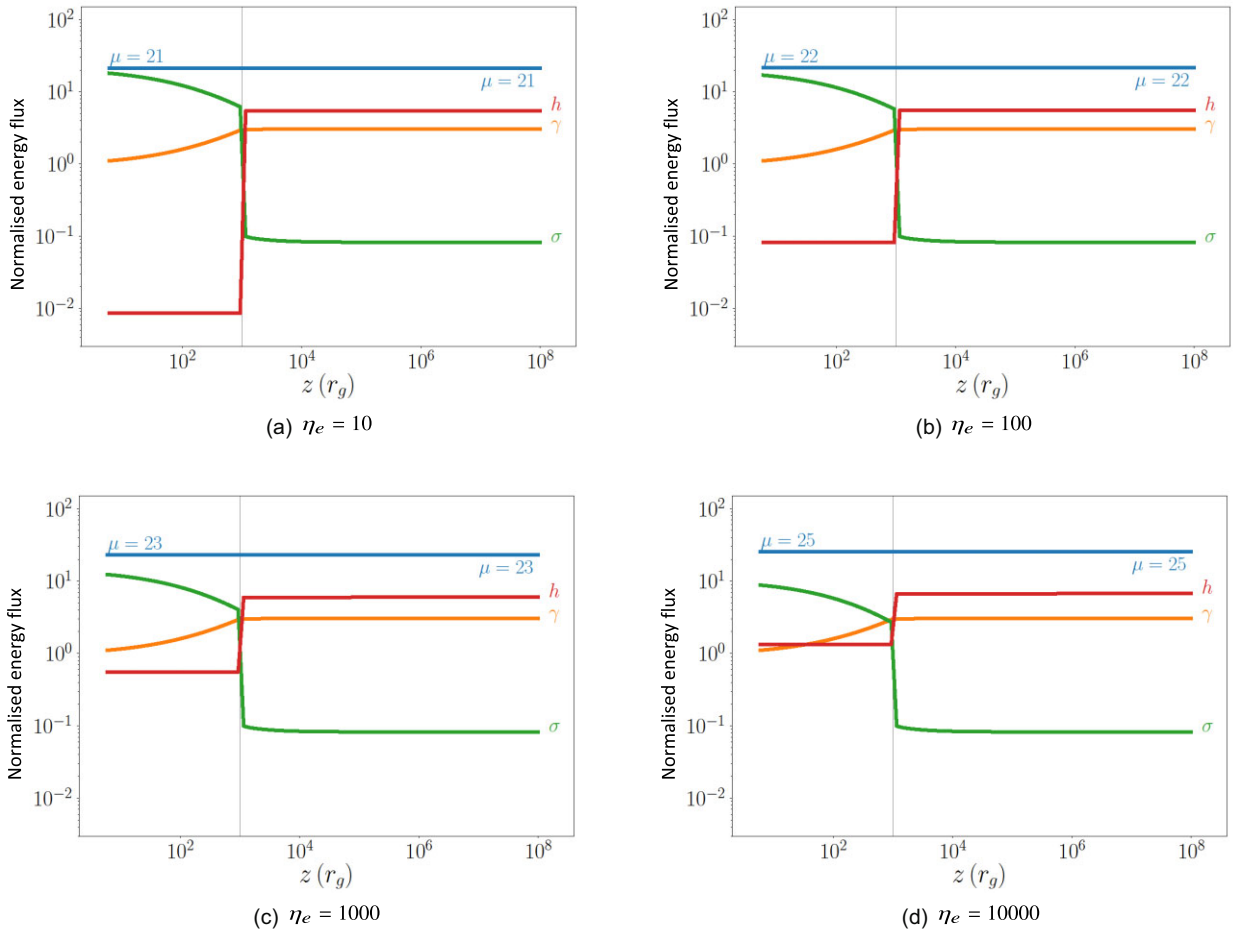

Figure B3. Same as Fig. B1 but for $\langle \varepsilon_e \rangle = 6$. We further account for hadronic acceleration with $\langle \varepsilon_p \rangle = 4$.

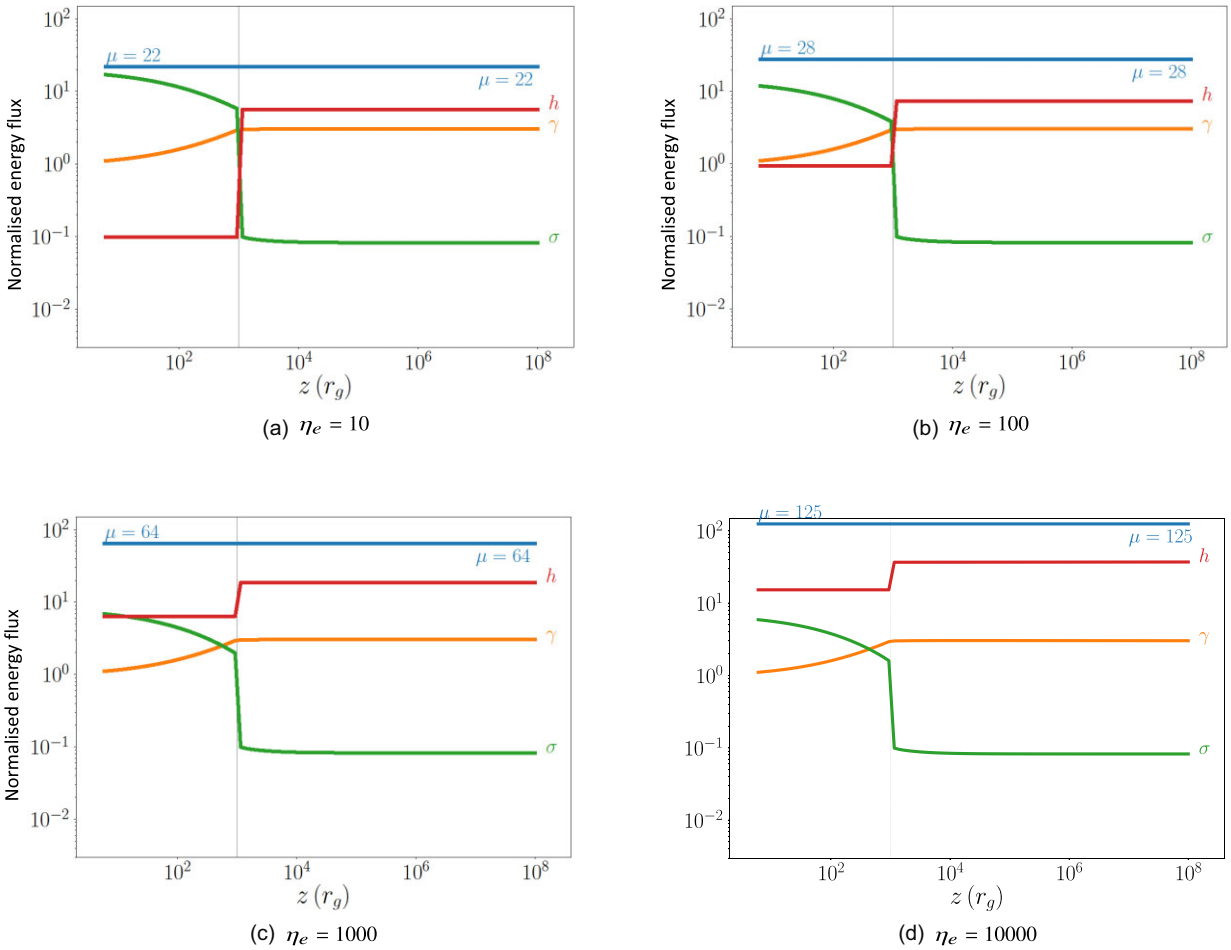

Figure B4. Same as Fig. B3 but for $\langle \varepsilon_e \rangle = 32$ and $\langle \varepsilon_p \rangle = 4$.

APPENDIX C: ARTIFICIAL MASS-LOSS

In Fig. C1, we show how the increase of the specific enthalpy h in the mass loading region may lead to a unphysical increase of μ that would mean mass-loss instead. Such an artificial mass-loss is due to the fact that we assume a hot flow and/or a pair dominated jet base with $\eta_e \gg 1000$. To avoid such a condition, we first calculate the value of μ from the 5$^{\rm th}$ order polynomial

$$\log_{10}(\mu) = 0.2231\,x^5 - 0.7242\,x^4 + 0.4546\,x^3 + 0.104\,x^2 - 0.09267\,x + 1.031, \quad \text{(C1)}$$

based on the results of CLTM19, and then we calculate h from the equation $h = \mu/\gamma - (\sigma + 1)$, where the values of γ and σ are from equations (29) and 28, respectively. In the cases that the specific enthalpy h would drop to zero (see for instance Figs C1 and C2), we choose to set h to a very low value, namely 1 per cent of the magnetisation. In the above equation, x is the same as in Section 4.

Finally, in Fig. C2 we plot the scenario where the artificial mass-loss is due to a combination of a large Lorentz factor ($\gamma_{\rm acc} = 10$) and the profile of h from equation (30). The above assumption allows forcing a mass-loading scenario.

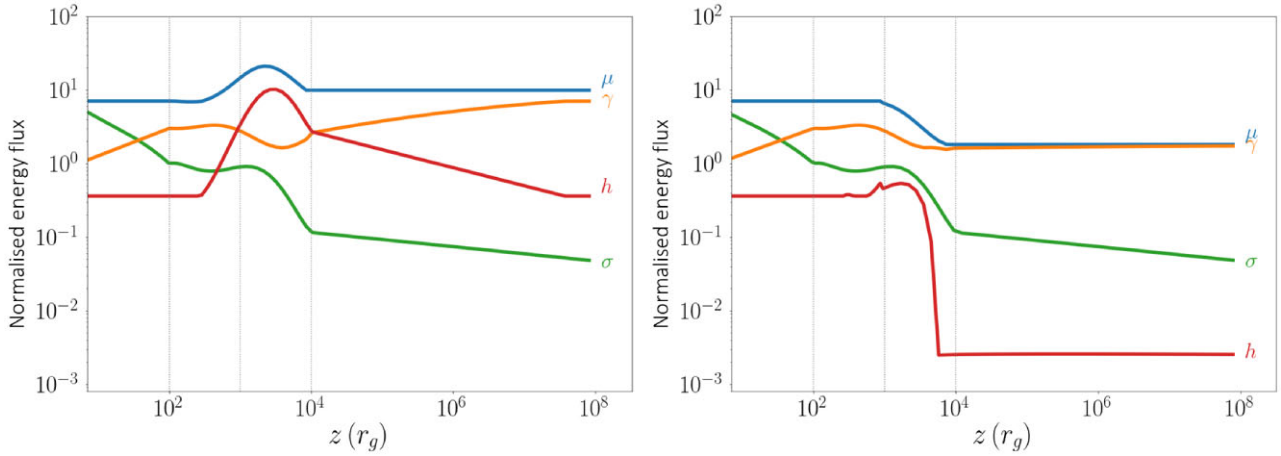

Figure C1. The jet energy components similar to Fig. 6 but for the case of a jet base with $\eta_e = 10^5$. Following the description we discuss in Section 4, the particular profile of h leads to an artificial increase of μ that would mean mass-loss instead, which is unphysical (*left*). Using the profile of μ from equation (C1), we constrain h to follow the mass-loading scenario (*right*). The initial magnetisation is $\sigma_0 = 5$ and the Lorentz factor at the dissipation region is $\gamma_{\rm acc} = 3$.

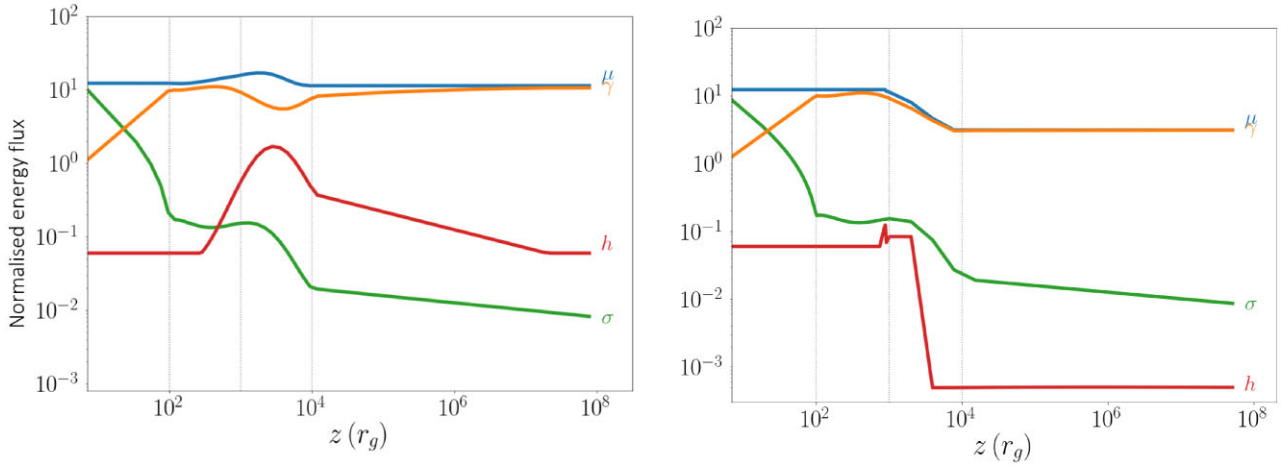

Figure C2. Similar to Fig. C1 but for the case of $\gamma_{\rm acc} = 10$, $\sigma_0 = 10$, and $\eta_e = 10^4$.

APPENDIX D: SED COMPONENTS

In Fig. D1, we show the spectrum as presented on the right subplot of Fig. 8 but with the individual components instead.

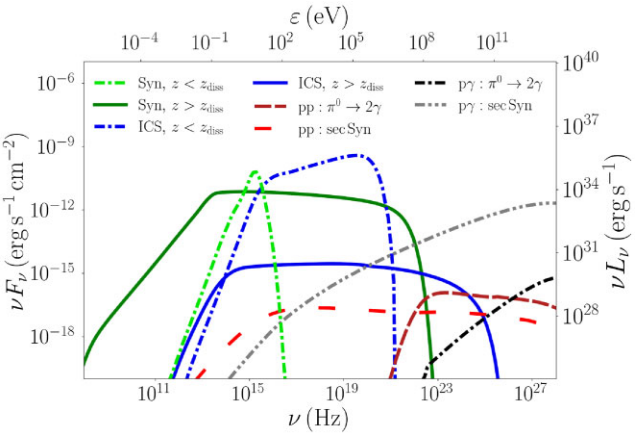

Figure D1. Identical to the right subplot of Fig. 8, but in this plot we show the individual radiative components as indicated in the legend.

APPENDIX E: PROTON POWER

In Fig. E1, we plot the fraction of the energy that is allocated to proton acceleration with respect to the total available energy flux of the jet μ. We plot this quantity versus the total specific enthalpy of the jet h for different average Lorentz factors $\langle \varepsilon_e \rangle$ of the electrons. In the main text, we included the case where $\eta_e = 10$, and here we plot the cases where $\eta_e = 1$ (*left*) and $\eta_e = 100$ (*right*), for completeness. See Section 6.3 for further information.

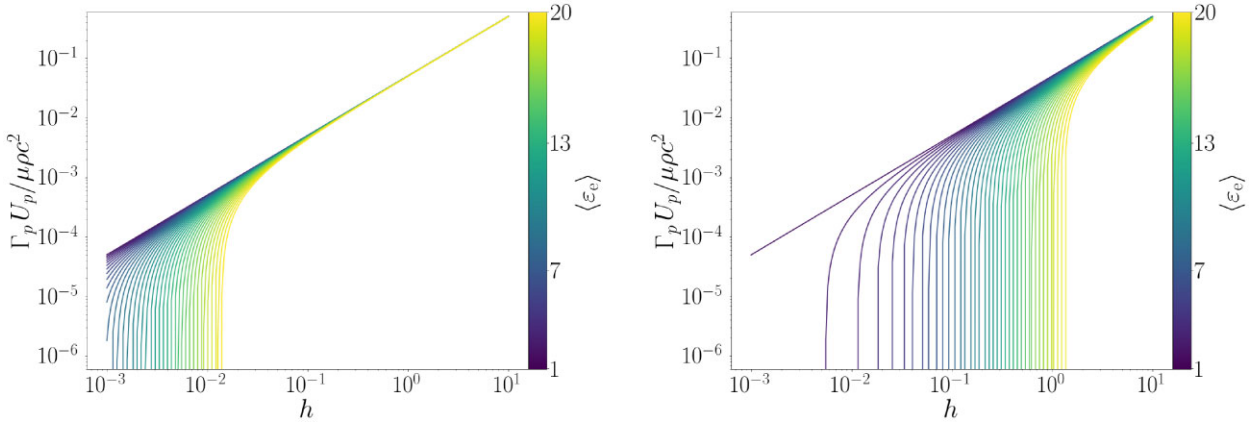

Figure E1. The specific enthalpy of the protons $\Gamma_p U_p/\rho c^2$ divided by μ shows the total energy that is allocated to protons with respect to the total available jet energy, as a function of the jet specific enthalpy h. We plot the proton energy density for a number of different electron energy densities that correspond to different values of $\langle\varepsilon_e\rangle$ as shown in the colour map, and we use $\eta_e = 1$ in the *left*, and $\eta_e = 100$ in the *right*.

This paper has been typeset from a TEX/LATEX file prepared by the author.